iScience

CellPress
OPEN ACCESS

Article

Tailored Alkali Resistance of DeNO$_x$ Catalysts by Improving Redox Properties and Activating Adsorbed Reactive Species

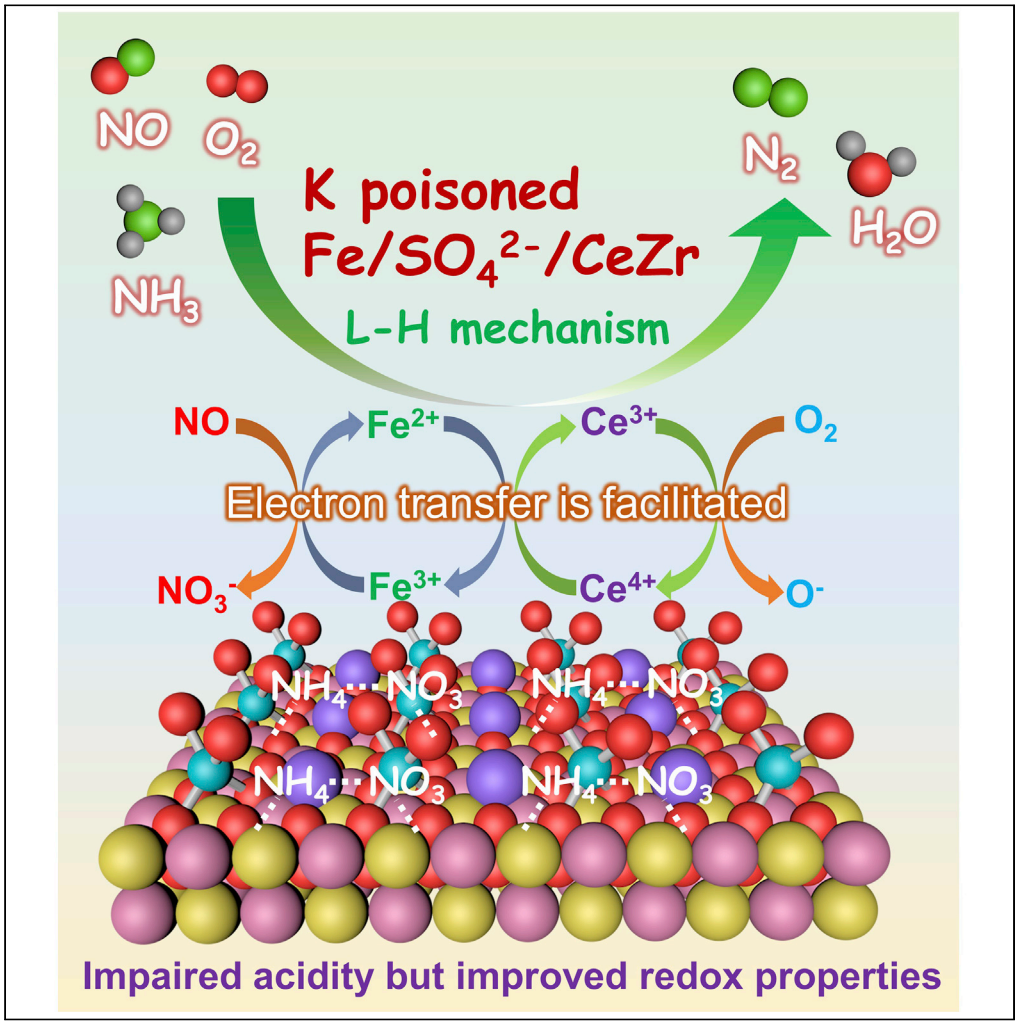

Mehak Nawaz Khan, Lupeng Han, Penglu Wang, Dengsong Zhang

dszhang@shu.edu.cn

HIGHLIGHTS

Fe-decorated SO_4^{2-}-modified CeZr catalysts exhibit superior alkali resistance

Improved redox properties compensate for the loss of the acidity

Higher reactivity of NH_x species makes up their decreased quantity

Alkali resistance is enhanced via improving the redox and reactivity of NH_x species

Khan et al., iScience *23*, 101173
June 26, 2020
https://doi.org/10.1016/j.isci.2020.101173

iScience

CellPress
OPEN ACCESS

Article

Tailored Alkali Resistance of $DeNO_x$ Catalysts by Improving Redox Properties and Activating Adsorbed Reactive Species

Mehak Nawaz Khan,[1,2] Lupeng Han,[1,2] Penglu Wang,[1] and Dengsong Zhang[1,3,*]

SUMMARY

It is still challenging to develop strongly alkali-resistant catalysts for selective catalytic reduction of NO_x with NH_3. It is generally believed that the maintenance of acidity is the most important factor because of neutral effects of alkali. This work discovers that the redox properties rather than acidity play decisive roles in improving alkali resistance of some specific catalyst systems. K-poisoned Fe-decorated SO_4^{2-}-modified CeZr oxide ($Fe/SO_4^{2-}/CeZr$) catalysts show decreased acidity but reserve the high redox properties. The higher reactivity of NH_x species induced by K poisoning compensates for the decreased amount of adsorbed NH_x, leading to a desired reaction efficiency between adsorbed NH_x and nitrate species. This study provides a unique perspective in designing an alkali-resistant $deNO_x$ catalyst via improving redox properties and activating the reactivities of NH_x species rather than routinely increasing acidic sites for NH_x adsorption, which is of significance for academic interests and practical applications.

INTRODUCTION

Concerns about the severe acid rain and haze problems caused by NO_x excessive emission have triggered extensive researches on effective abatement controls of NO_x ($deNO_x$) via NH_3 selective catalytic reduction (NH_3-SCR) (Han et al., 2019a, 2019c; Paolucci et al., 2017; Qu et al., 2020). Since the ultra-low emissions of NO_x have been almost attained for the power plants, it is more pressing to reduce NO_x emissions in some non-electrical industries such as steel plants, biomass burning boilers, and waste incinerators. There is an increasing demand for novel alkali-resistant SCR catalysts because the commercial vanadia-based catalysts tend to be poisoned by the alkali metals such as K and Na released from the flue gas (Hao et al., 2019; Huang et al., 2013; Marberger et al., 2016; Peng et al., 2016). A generally recognized deactivation mechanism is the proton exchange of alkali-metal ions onto the active Brønsted acid sites, which results in the loss of acidity over the neutralized acid sites (Hao et al., 2019; Hu et al., 2015b). A feasible approach to improve the alkali tolerance is adopting strongly acidic supports that supply sufficient acidic sites to interact with alkali ions and thus protect the active sites. Sulfated metal oxides supports such as TiO_2 and ZrO_2 as well as sulfated titanate nanotubes have effectively improved alkali resistance (Due-Hansen et al., 2007; Gao et al., 2014; Putluru et al., 2012; Wang et al., 2015). However, this approach impairs the catalytic activity to some extent because of the sacrificial acidity of acidic supports. Another efficient strategy of alkali resistance is constructing the alkali-trapping sites that separate active sites and alkali-poisoned sites. Such a measure could reserve the original activity of catalysts on account of the intact acidic and redox sites. Hollandite manganese oxide and hexagonal WO_3 have been demonstrated to be effective for strengthening alkali resistance owing to the trapping effects of internal tunnels without destroying active sites (Hu et al., 2015b; Zheng et al., 2016). These strategies could protect active sites from alkali poisoning through precise structural designs. However, the stringent specification of acidity strength, pore tunnels, and type of oxides restrict the alkali-resistant applications. Actually, the alkali-resistant strategy is still lacking to develop highly efficient catalysts.

So far, less research effort has been devoted to the variation of redox sites and the reactivity of adsorbed nitrate and NH_x species associated with alkali poisoning, which are decisive to SCR activity. In this study, we discover an unexpected result that redox properties rather than acidity play decisive roles in improving alkali resistance of Fe-decorated SO_4^{2-}-modified CeZr oxide ($Fe/SO_4^{2-}/CeZr$) catalysts. Herein, Ce-Zr mixed

[1]State Key Laboratory of Advanced Special Steel, School of Materials Science and Engineering, Research Center of Nano Science and Technology, Department of Chemistry, College of Sciences, Shanghai University, Shanghai 200444, China

[2]These authors contributed equally

[3]Lead Contact

*Correspondence: dszhang@shu.edu.cn

https://doi.org/10.1016/j.isci.2020.101173

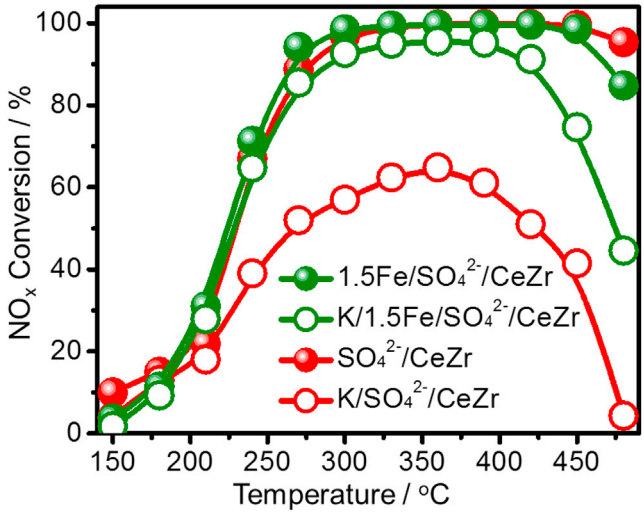

Figure 1. NO Conversion during the SCR Reaction over Various Catalysts.
Reaction conditions: 500 ppm NO, 500 ppm NH_3, 5 vol % O_2, N_2 as the balance gas, and GHSV of 100,000 h^{-1}.

oxides combining the highly refractory property of ZrO_2 with the superior oxygen storage capacity of CeO_2 are used as the model catalyst, which are usually served as supports for SCR catalysts (Ding et al., 2015; Li et al., 2008; Sánchez Escribano et al., 2009). SO_4^{2-} modification is performed on Ce-Zr mixed oxides to increase the acidic sites and improve the SCR activity (Zhang et al., 2017), whereas the SCR activity of SO_4^{2-}/CeZr is largely decreased after alkali poisoning because of the loss of acidity and redox properties associated with the decreased reactivity of adsorbed nitrate and NH_x species. Via decorating Fe on SO_4^{2-}/CeZr, the redox properties are enhanced after K poisoning owing to the promoted electron transfer between K, Fe, Ce, and Zr as well as sufficient Ce^{3+} and active oxygen species. Although the acid amount of K/Fe/SO_4^{2-}/CeZr catalysts decreases more severely than K/SO_4^{2-}/CeZr, the enhanced redox properties compensate for the loss of acidity, which notably improves the reactivity of adsorbed NH_x and meanwhile maintains the high reactivity of adsorbed nitrate species. Therefore, the K-poisoned Fe/SO_4^{2-}/CeZr catalyst exhibits satisfactory SCR activity. This finding is of significance in revealing novel alkali-resistant mechanisms and paves a novel way for developing alkali-resistant catalysts in the future research.

RESULTS

Originally, one strategy of increasing acidity was attempted to improve the SCR activity via introducing SO_4^{2-} onto the surface of CeZr oxides. As expected, SO_4^{2-}/CeZr shows higher SCR activity (300°C–480°C, NO conversion above 90%, Figure 1) compared with the pristine CeZr mixed oxides (the highest NO conversion of 80% at 330°C, Figure S1). K-poisoned CeZr catalyst is almost deactivated with the highest NO conversion of only 16.7% at 360°C (Figure S1) and K-poisoned SO_4^{2-}/CeZr catalyst also displays poor activity with the maximum 64.8% NO conversion at 360°C (Figure 1). This result indicates that introducing more acidic sites is not enough to maintain the SCR activity of CeZr catalysts after K poisoning. Besides, Fe-decorated CeZr (without SO_4^{2-} modification) shows lower activity than SO_4^{2-}/CeZr and inferior K resistance because of the less acidity (Figure S2). Via tuning the amount of Fe decoration on SO_4^{2-}/CeZr, 1.5Fe/SO_4^{2-}/CeZr exhibits the optimum SCR activity with a broad temperature window (270°C–450°C, NO conversion above 90%) (Figure S3). After K poisoning, 1.5Fe/SO_4^{2-}/CeZr still exhibits more than 85% NO conversion within 270°C–420°C (Figure 1), indicating that Fe decoration notably improves the alkali resistance of SO_4^{2-}/CeZr. Besides, the fresh/K-poisoned SO_4^{2-}/CeZr and 1.5Fe/SO_4^{2-}/CeZr catalysts all show good N_2 selectivity above 90% within 150°C–480°C (Figure S4).

To probe the effects of Fe decoration on the alkali resistance of SO_4^{2-}/CeZr, the structural and textural features of fresh and K-poisoned SO_4^{2-}/CeZr and 1.5Fe/SO_4^{2-}/CeZr were first investigated. The X-ray diffraction patterns (Figure S5) and Raman spectra (Figure S6) both evidence the formation of Ce-Zr solid solution over fresh/K-poisoned SO_4^{2-}/CeZr and 1.5Fe/SO_4^{2-}/CeZr catalysts. Besides, no FeO_x-related X-ray diffraction peaks or Raman bands are observed, indicating the FeO_x is highly dispersed on the surface of SO_4^{2-}/CeZr. The scanning electron microscope mapping of the representative K-poisoned 1.5Fe/SO_4^{2-}/CeZr catalyst shows that Fe,

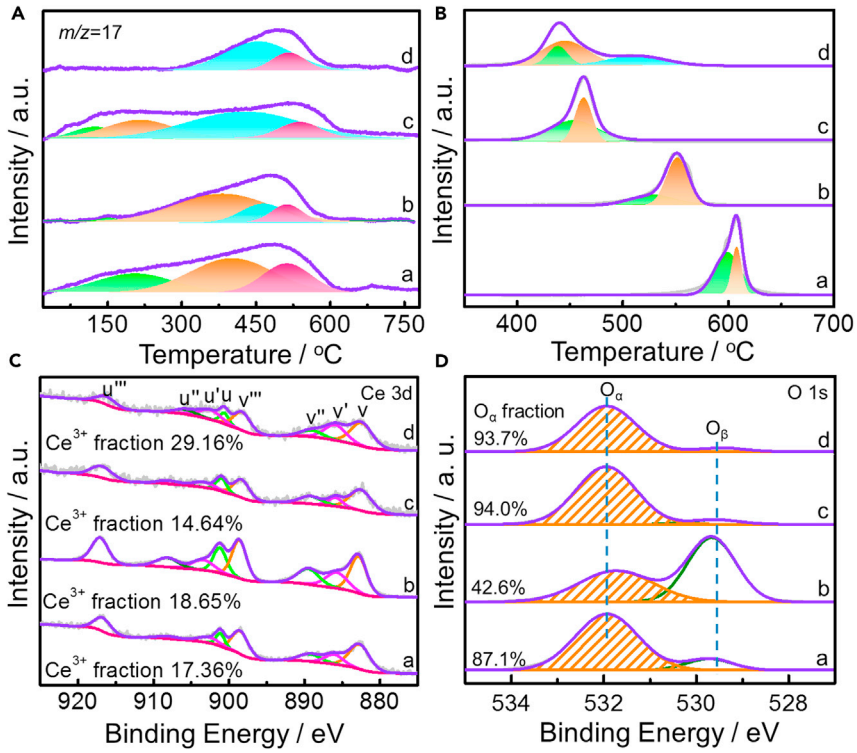

Figure 2. Acidity and Redox Properties of Different Catalysts

(A) NH_3-TPD-MS, (B) H_2-TPR, (C) XPS spectra of Ce 3d, and (D) XPS spectra of O 1s over different catalysts. Catalysts: SO_4^{2-}/CeZr (a), K/SO_4^{2-}/CeZr (b), 1.5Fe/SO_4^{2-}/CeZr (c), and K/1.5Fe/SO_4^{2-}/CeZr (d).

Ce, and Zr active components are highly dispersed with each other and K is also uniformly dispersed on the surface of catalysts (Figure S7). The Brunauer-Emmett-Teller (BET) surface areas of fresh SO_4^{2-}/CeZr and 1.5Fe/SO_4^{2-}/CeZr are 60.06 and 44.42 m^2/g, whereas they increase to 70.37 and 66.29 m^2/g after K poisoning, respectively. The increase of surface area after K poisoning is likely due to the contribution of K_2O nanoparticle on catalyst surface (Table S1). There is no correlation between surface area and SCR activity, indicating that the surface area of catalysts is not decisive to the SCR activity of catalysts.

The exposure of catalysts to alkali metals could reduce the acid sites for NH_3 adsorption/activation, thus causing a severe decrease of catalytic activity. It is necessary to probe the changes in acidity of SO_4^{2-}/CeZr and 1.5Fe/SO_4^{2-}/CeZr catalysts before/after K poisoning. Herein, NH_3 temperature-programmed desorption combining with mass spectrum (NH_3-TPD-MS) was performed to study the acidic properties of catalysts (Figure 2A). The NH_3 desorption peaks below 300°C on all the catalysts are attributed to the weakly acidic sites, and the peaks above 300°C are attributed to the strongly acidic sites (Park et al., 2016). K poisoning obviously decreases the amount of weakly acidic sites over SO_4^{2-}/CeZr and 1.5Fe/SO_4^{2-}/CeZr. The quantitative analysis of NH_3-TPD-MS reveals that the total acid amount of SO_4^{2-}/CeZr decreases from 292.2 to 182.9 μmol/g (decrease by 37.4%), whereas that of 1.5Fe/SO_4^{2-}/CeZr decreases from 257.6 to 115.2 mmol/g (decrease by 55.3%) after K poisoning. The fresh 1.5Fe/SO_4^{2-}/CeZr (257.6 μmol/g) owns less acidity than the fresh SO_4^{2-}/CeZr (292.2 μmol/g) likely because FeO_x species occupy some SO_4^{2-} acidic sites. The acid amount of 1.5Fe/SO_4^{2-}/CeZr decreases more severely than SO_4^{2-}/CeZr (decrease by 55.3% versus 37.4%) after K poisoning, which is likely because more weakly acidic sites derived from Fe-OH are lost (Sugawara et al., 2007). This is also evidenced by that K/1.5Fe/SO_4^{2-}/CeZr almost lost all the weak acid but K/SO_4^{2-}/CeZr still possesses some weak acid (Figure 2A). It is notable that the total acid amount of K/1.5Fe/SO_4^{2-}/CeZr is even less than K/SO_4^{2-}/CeZr, implying that the acid amount is not the essential reason for the strong K resistance of 1.5Fe/SO_4^{2-}/CeZr catalysts. Besides, SO_2 signal (m/z = 64) was observed above 600°C over all fresh and K-poisoned catalysts during NH_3-TPD-MS (Figure S8), indicating that SO_4^{2-} strongly bonds on CeZr catalysts and is thermally stable during the whole SCR active temperature region (<500°C).

As mentioned above, the acid amount is notably reduced for K-poisoned 1.5Fe/SO_4^{2-}/CeZr. One question arises: Does the increased redox property associated with Fe decoration improve the alkali resistance? To check the changes of redox properties along with Fe decoration, H_2 temperature-programmed reduction (H_2-TPR) and X-ray photoelectron spectroscopy (XPS) were carried out for Fresh and K-poisoned catalysts. As shown in Figure 2B, SO_4^{2-}/CeZr shows two fitted reduction peaks around 600°C, which are related to the reduction of CeO_x that is not interacted with ZrO_x (low-temperature peak) and CeO_x that is strongly interacted with ZrO_x (high-temperature peak), respectively. After K poisoning, the two reduction peaks of SO_4^{2-}/CeZr shift to lower temperatures (around 540°C), which implies K as an electron donating promoter facilitates the CeO_2 reduction. Compared with SO_4^{2-}/CeZr, the two fitted reduction peaks of 1.5Fe/SO_4^{2-}/CeZr shift to much lower temperatures (around 450°C), in which the low-temperature peak is likely related to the FeO_x reduction and the high-temperature one is attributed to the CeO_x reduction (Liu and He, 2010). With increasing the amount of Fe to 3 wt % Fe and 5 wt % Fe, the reduction peaks further shift to lower temperatures of ~440°C and ~420°C, respectively (Figure S9). These results indicate that the strong interaction between Fe and Ce facilitates the reduction of CeO_2. The reduction peaks of FeO_x/CeO_x of 1.5Fe/SO_4^{2-}/CeZr catalysts after K poisoning shift from ~450°C to ~440°C, and the third reduction peak around 510°C appears, indicating that K poisoning improves the reduction of FeO_x/CeO_x species but meanwhile impairs the interaction between Fe and Ce to some extent, which restrains the reduction of CeO_x. The reduction of CeO_x over K poisoned 1.5Fe/SO_4^{2-}/CeZr is still more reducible compared with K-poisoned SO_4^{2-}/CeZr according to the highest reduction temperature of CeO_x (510°C for K/1.5Fe/SO_4^{2-}/CeZr versus 550°C for K/SO_4^{2-}/CeZr). These indicate that the reducibility is improved over Fe-decorated SO_4^{2-}/CeZr catalysts and K poisoning further enhances the reducibility to some extent. Via analyzing X-ray photoelectron spectroscopy (XPS) of Ce 3d, K-poisoned SO_4^{2-}/CeZr and 1.5Fe/SO_4^{2-}/CeZr both show higher Ce^{3+}/(Ce^{3+}+Ce^{4+}) ratio than fresh ones (Figure 2C) (Han et al., 2019b), which is attributed to that K as an electron donating promoter reduces the valence of Ce species. Although the fresh 1.5Fe/SO_4^{2-}/CeZr has less Ce^{3+} fraction than SO_4^{2-}/CeZr, the K-poisoned 1.5Fe/SO_4^{2-}/CeZr shows the highest Ce^{3+} fraction of 29.2%, which indicates that the electron-donating effects of K also facilitate the electron transfer from Fe to Ce. Generally, the formation of Ce^{3+} species brings out more oxygen vacancies, and the higher Ce^{3+} ratio with the more oxygen vacancies improves the oxidizability. Moreover, the surface oxygen species also deliver a different evolution after K poisoning. It is generally recognized that the surface-adsorbed oxygen species (denoted as O_α) are much more reactive in SCR reactions than the lattice oxygen species (denoted as O_β). As seen in Figure 2D, the $O_\alpha/(O_\alpha+O_\beta)$ ratio of SO_4^{2-}/CeZr significantly decreases from 87.1% to 42.6% after K poisoning, whereas the $O_\alpha/(O_\alpha+O_\beta)$ ratio of K-poisoned 1.5Fe/SO_4^{2-}/CeZr keeps at 93.7% that is almost unchanged with the fresh one (94.0%). This indicates that Fe decoration maintains the surface adsorption oxygen species that are active for the oxidation process for the SCR reaction. The O_2-TPD results also evidence that the chemically adsorbed oxygen molecule anion (O_2^-) and oxygen anion (O^-) species are notably reduced over K-poisoned SO_4^{2-}/CeZr but almost unchanged over K-poisoned 1.5Fe/SO_4^{2-}/CeZr (Figure S10). The electron states of Fe, Zr, and S for alkali-poisoned SO_4^{2-}/CeZr and 1.5Fe/SO_4^{2-}/CeZr were also investigated. As the weak Fe 2p XPS signals of 1.5Fe/SO_4^{2-}/CeZr and K/1.5Fe/SO_4^{2-}/CeZr (Figure S11A), the Fe 2p XPS spectra of 5Fe/SO_4^{2-}/CeZr before/after K poisoning were analyzed (Figure S11B). The fresh 5Fe/SO_4^{2-}/CeZr possesses more Ce^{3+} fraction (22.97%) than the fresh 1.5Fe/SO_4^{2-}/CeZr (14.64%), indicating more electron transfer from Fe to Ce. Additionally, K-poisoned 5Fe/SO_4^{2-}/CeZr possesses higher Fe^{2+}/(Fe^{2+} + Fe^{3+}) ratio and Ce^{3+} fraction than the fresh one owing to the electron-donating effects of K. 1.5Fe/SO_4^{2-}/CeZr has higher binding energy of Zr $3d_{5/2}$ than SO_4^{2-}/CeZr (Figure S12), indicating Fe likely gets electron from Zr owing to the strong interaction between Fe and Zr. After K poisoning, the Zr $3d_{5/2}$ binding energy of both catalysts shifts to a lower value due to the electron-donating effects of K. Additionally, K poisoning does not change the valence of S species, which exist in SO_4^{2-} species on all fresh and K-poisoned catalysts (Figure S13). Based on the above results, K-poisoned 1.5Fe/SO_4^{2-}/CeZr improves the reducibility and maintains the high oxidative capacity because of the facilitated electron transfer between K, Fe, Ce, and Zr as well as adequate Ce^{3+} and active oxygen species. As a comparison, the reducibility of K-poisoned SO_4^{2-}/CeZr is not as good as K-poisoned 1.5Fe/SO_4^{2-}/CeZr and the oxidative capacity of K-poisoned SO_4^{2-}/CeZr is largely impaired owing to the notable decrease of active oxygen species. Therefore, the K-poisoned 1.5Fe/SO_4^{2-}/CeZr shows stronger redox properties than K-poisoned SO_4^{2-}/CeZr.

It has been demonstrated that the acidity decreases but the redox properties reserve over K-poisoned 1.5Fe/SO_4^{2-}/CeZr catalysts. Why can the K/1.5Fe/SO_4^{2-}/CeZr catalyst maintain high activity in spite of the decreased acidity? Differences in the reactivity of adsorbed NH_x and nitrate species may be the possible reason. Therefore, the adsorption and activation characteristics of NH_3 and NO need to be probed. From the *in situ* DRIFTs of NH_3 desorption under various temperatures (Figure S14), the NH_4^+ and NH_3 species adsorbed on both SO_4^{2-}/CeZr and 1.5Fe/SO_4^{2-}/CeZr catalysts are not stable and easy

to desorb above 250°C. The NH_4^+ (1,698, 1,472, and 1,438 cm^{-1}) (Huang et al., 2016, 2017; Wei et al., 2016) and NH_3 (1,369 cm^{-1}) (Zhang et al., 2018) species still exist on K-poisoned SO_4^{2-}/CeZr at 300°C (Figures 3A and 3A1), indicating that the adsorption strength of these NH_x species becomes stronger after K poisoning. By comparison, fewer NH_4^+ and NH_3 species adsorb on K/1.5Fe/SO_4^{2-}/CeZr at 300°C (Figures 3B and 3B1), implying that these NH_x species are likely more reactive because of their appropriate bonding strength. Additionally, *in situ* DRIFTs of NO + O_2 desorption under various temperatures were studied to investigate the adsorbed strength of NO_x species. It can be seen that the N_2O_4, bidentate nitrate, monodentate nitrite, and metal-NO_2 species adsorb on SO_4^{2-}/CeZr (Figure S15A), whereas the N_2O_4, bridged nitrate, and bidentate nitrate species adsorb on Fe-decorated SO_4^{2-}/CeZr catalysts (Figure S15B). With increasing temperatures, the NO_x species adsorbed on 1.5Fe/SO_4^{2-}/CeZr are easier to desorb than on SO_4^{2-}/CeZr, implying these species could react with NH_x species more easily. After K poisoning, K/SO_4^{2-}/CeZr catalysts show adsorbed NO_x species including N_2O_4 (1,713 cm^{-1}) (Davydov, 2003), adsorbed NO_2 (1,629 cm^{-1}) (Liu et al., 2017), bidentate nitrate (1,498 cm^{-1}) (Davydov, 2003), and metal-NO_2 (1,367 and 1,333 cm^{-1}) (Davydov, 2003) (Figures 3C and 3C1). It is notable that the bidentate nitrate and metal-NO_2 species still adsorb on K/SO_4^{2-}/CeZr at 300°C and the strong bonding with catalyst likely reduces their reactivity. By comparison, the N_2O_4 (1,707 cm^{-1}), bidentate nitrate (1,517 cm^{-1}) (Davydov, 2003), and metal-NO_2 (1,330 cm^{-1}) (Davydov, 2003) species on K-poisoned 1.5Fe/SO_4^{2-}/CeZr desorb more easily than those on K-poisoned SO_4^{2-}/CeZr catalysts (Figures 3D and 3D1). These results indicate that the reactivities of NO_x species over K-poisoned 1.5Fe/SO_4^{2-}/CeZr are likely higher than those over K-poisoned SO_4^{2-}/CeZr. Moreover, NO-TPD-MS (Figure S16A) and NO + O_2-TPD-MS (Figure S16B) results show that the amount of nitrate species adsorbed on SO_4^{2-}/CeZr reduces after K poisoning, whereas those on 1.5Fe/SO_4^{2-}/CeZr increases after K poisoning. This indicates that Fe decoration helps to improve the formation of nitrite species over K-poisoned catalysts, which is likely due to the improvement of redox properties after K poisoning.

In order to further reveal the changes in the reactivity of adsorbed NH_x and NO_x, *in situ* DRIFTs transient reactions of adsorbed species were investigated at 250°C. Before K poisoning, the bidentate nitrates and metal-NO_2 species adsorbed on SO_4^{2-}/CeZr and the N_2O_4, bidentate nitrates, and metal-NO_2 species adsorbed on 1.5Fe/SO_4^{2-}/CeZr are all reactive upon introducing NH_3 (Figures S17A and S17B). Notably, the reactivity of nitrate species on 1.5Fe/SO_4^{2-}/CeZr is much higher than that on SO_4^{2-}/CeZr. The adsorbed NH_4^+ and NH_3 species on fresh SO_4^{2-}/CeZr and 1.5Fe/SO_4^{2-}/CeZr decrease slowly upon introducing NO + O_2, indicating the reactivity of NH_x species over both catalysts are all relatively inactive, whereas the reactivity of NH_x species on 1.5Fe/SO_4^{2-}/CeZr is slightly higher than that on SO_4^{2-}/CeZr (Figure S18A and S18B). These results imply that Fe decoration relatively improves the reactivities of adsorbed nitrate and NH_x species. After K poisoning (Figures 4A and 4A1), the N_2O_4 (1,696 cm^{-1}), bidentate nitrates (1,562 cm^{-1}) (Liu et al., 2017), and metal-NO_2 (1,384 cm^{-1}) (Davydov, 2003) species adsorbed on K/SO_4^{2-}/CeZr decrease slowly and meanwhile the NH_4^+ (1,680 and 1,423 cm^{-1}) (Ma et al., 2014) and NH_3 (1,583 cm^{-1}) (Weng et al., 2016) species gradually increase with introducing NH_3, indicating the reactivity of nitrate species largely decreases compared with the fresh one. In contrast, the adsorbed bidentate nitrates (1,573, 1,559 cm^{-1}) (Hu et al., 2015a; Liu et al., 2018) and metal-NO_2 (1,381, 1,368 cm^{-1}) (Davydov, 2003) species on K/1.5Fe/SO_4^{2-}/CeZr reduce notably with the introduction of NH_3, and meanwhile amide-like species (1,724 cm^{-1}) (Jeong et al., 2017) and NH_4^+ species (1,678 cm^{-1}) (Weng et al., 2016) emerge (Figures 4B and 4B1). These results indicate that K poisoning decreases the reactivity of nitrate species over SO_4^{2-}/CeZr but has less impact on that over 1.5Fe/SO_4^{2-}/CeZr. In terms of the reactivity of NH_x species on K/SO_4^{2-}/CeZr (Figures 4C and 4C1), the adsorbed amide-like species (1,724 cm^{-1}) (Jeong et al., 2017), NH_4^+ (1,680 and 1,630 cm^{-1}) (Yu et al., 2014) and NH_3 species (1,362 and 1,332 cm^{-1}) (Zhang et al., 2018) are almost unchanged upon introducing NO + O_2, and meanwhile the metal-NO_2 species that overlap with the NH_3 species gradually increase with the introduction of NO + O_2. By comparison, the adsorbed NH_4^+ (1,678, 1,654, and 1,434 cm^{-1}) (Weng et al., 2016) and NH_3 (1,375 cm^{-1}) (Wang et al., 2016) species on K-poisoned 1.5Fe/SO_4^{2-}/CeZr notably reduce with the introduction of NO + O_2 (Figures 4D and 4D1). Meanwhile, the metal-NO_2 (1,367 cm^{-1}) species increase with continuously introducing NO + O_2 (Figures 4D and 4D1). These indicate that the adsorbed NH_x species on SO_4^{2-}/CeZr become more inactive after K poisoning; however, the adsorbed NH_x species on K-poisoned 1.5Fe/SO_4^{2-}/CeZr become more reactive with the adsorbed nitrate species compared with the fresh one. Overall, both fresh SO_4^{2-}/CeZr and 1.5Fe/SO_4^{2-}/CeZr conduct the SCR reaction through the reaction between adsorbed nitrate species and adsorbed NH_x species following the Langmuir-Hinshelwood (L-H) mechanism. In this reaction pathway, the reactivity of NH_x species over both fresh catalysts are relatively inactive. After K poisoning, the reactivity of NH_x and nitrate species largely decreases on SO_4^{2-}/CeZr, leading to an inferior alkali

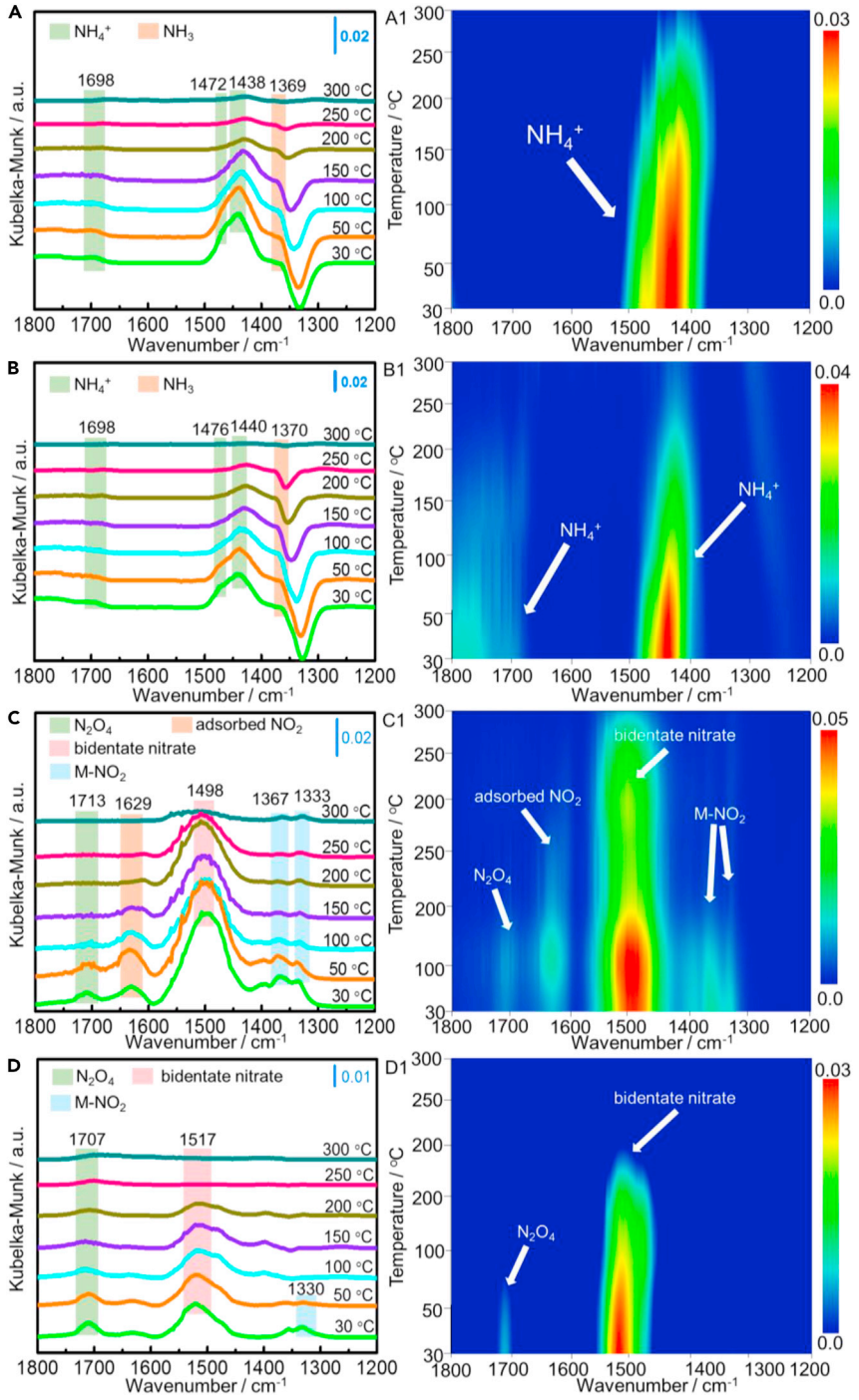

Figure 3. *In situ* DRIFTs of NH_x/NO_x Species Desorption over Catalysts as a Function of Temperature

In situ DRIFTs of NH_3 desorption and the corresponding mapping results over $K/SO_4^{2-}/CeZr$ (A and A1) and $K/1.5Fe/SO_4^{2-}/CeZr$ (B and B1) catalysts after exposure to a flow of 500 ppm NH_3 for 1 h at 30°C; *in situ* DRIFTs of NO + O_2 desorption and the corresponding mapping results over $K/SO_4^{2-}/CeZr$ (C and C1) and $K/1.5Fe/SO_4^{2}/CeZr$ (D and D1) catalysts after exposure to a flow of 500 ppm NO + 5% O_2 for 1 h at 30°C.

resistance. However, K-poisoned $1.5Fe/SO_4^{2-}/CeZr$ reserves high reactivity of adsorbed nitrate species and especially largely improves the reactivity of adsorbed NH_x species. Consequently, $1.5Fe/SO_4^{2-}/CeZr$ exhibits a satisfactory alkali resistance in spite of the decreased acidic sites.

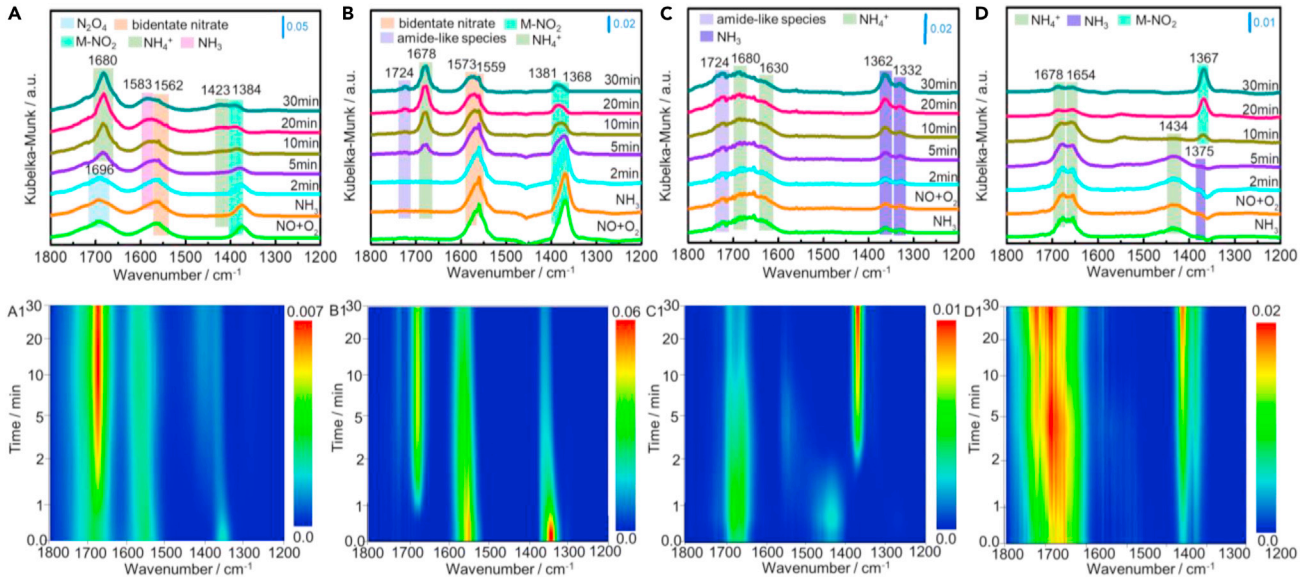

Figure 4. *In situ* DRIFTs of the Transient Reactions over $K/SO_4^{2-}/CeZr$ and $K/1.5Fe/SO_4^{2-}/CeZr$

In situ DRIFTs of the transient reactions between NH_3 and preadsorbed NO + O_2 over $K/SO_4^{2-}/CeZr$ (A and A1) and $K/1.5Fe/SO_4^{2-}/CeZr$ (B and B1) at 250°C as a function of time; *in situ* DRIFTs of the transient reactions between NO + O_2 and preadsorbed NH_3 over $K/SO_4^{2-}/CeZr$ (C and C1) and $K/1.5Fe/SO_4^{2-}/CeZr$ (D and D1) at 250°C as a function of time.

DISCUSSION

Nowadays, it is generally believed that the decrease in acidity is the dominant reason for the deactivation of catalysts after alkali poisoning (Hu et al., 2015b; Putluru et al., 2011; Wang et al., 2015). Additionally, the impaired redox properties resulting from alkali poisoning also lead to the decline of activity, such as the reduced reducibility for K-poisoned V_2O_5-WO_3/TiO_2 (Wang et al., 2019) and decreased oxidative capacity for K-poisoned Mn/TiO_2 (Wei et al., 2018). Besides the reduced acidity and redox properties, the absence of active NO_x species at low temperatures and the formation of inactive nitrate species at high temperatures result in the decreased activity of alkali-poisoned V_2O_5/CeO_2 (Peng et al., 2014). In this study, we found that the redox properties rather than acidity play decisive roles in improving the alkali resistance of some specific catalyst systems. It is demonstrated that the acid amount of K-poisoned $Fe/SO_4^{2-}/CeZr$ is lower than that of K-poisoned $SO_4^{2-}/CeZr$; however, the SCR activity of the former one is much higher than that of the latter one. The K-resistant mechanism of $F/SO_4^{2-}/CeZr$ is revealed as shown in Figure 5. The essential reason is that the enhanced redox properties compensate for the reduced acidity of the K-poisoned $Fe/SO_4^{2-}/CeZr$ catalysts. K-poisoned $Fe/SO_4^{2-}/CeZr$ facilitates the electron transfer between K, Fe, Ce, and Zr while reserving plenty of Ce^{3+} and active oxygen species, which improves the reducibility and reserves the high oxidative capacity. As a result, $K/Fe/SO_4^{2-}/CeZr$ maintains the high reactivity of adsorbed nitrate species and notably improves the reactivity of adsorbed NH_x species. The higher reactivity of NH_x species makes up for the loss in quantity of NH_x species, which is the key for the strong K resistance of $Fe/SO_4^{2-}/CeZr$. Consequently, $Fe/SO_4^{2-}/CeZr$ maintains the high reaction efficiency between adsorbed NH_x species and adsorbed nitrate species (L-H mechanism). Conversely, the acidity decreases and the redox circle is locked for the decreased oxidative capacity on $K/SO_4^{2-}/CeZr$, which largely reduces the reactivity of nitrate species and NH_x, leading to decreased activity. This work sheds light on a novel alkali-resistant mechanism via improving redox properties and activating the reactivities of NH_x species rather than routinely increasing acidic sites for NH_x adsorption. This study provides a unique perspective in designing an alkali-resistant deNO_x catalysts, which is beneficial for their commercial, environmental, and industrial applications.

Limitations of the Study

More catalyst systems should be probed that can improve their alkali resistance via improving redox properties and activating the reactivities of NH_x and nitrate species.

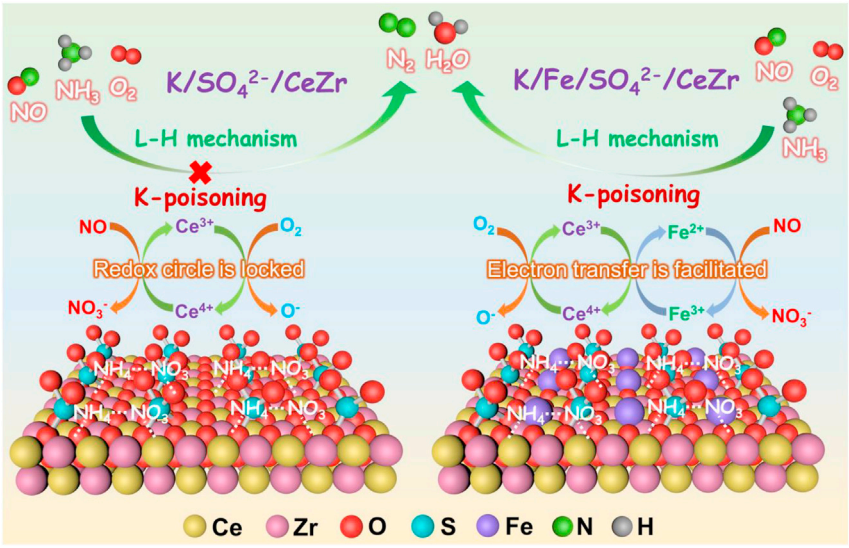

Figure 5. Schematic Diagram of the Deactivation Mechanism over $K/SO_4^{2-}/CeZr$ and Alkali-Resistant Mechanism over $K/Fe/SO_4^{2-}/CeZr$ Catalysts.

Resource Availability

Lead Contact

Further information and requests for resources and reagents should be directed to and will be fulfilled by the Lead Contact, Dengsong Zhang (dszhang@shu.edu.cn).

Materials Availability

All unique/stable reagents generated in this study are available from the Lead Contact without restriction.

Data and Code Availability

All relevant data are available from the corresponding author (dszhang@shu.edu.cn) upon reasonable request.

METHODS

All methods can be found in the accompanying Transparent Methods supplemental file.

SUPPLEMENTAL INFORMATION

Supplemental Information can be found online at https://doi.org/10.1016/j.isci.2020.101173.

ACKNOWLEDGMENTS

We acknowledge the support of the National Natural Science Foundation of China (21722704; 21976117; 21906102), the National Key R&D Program of China (2017YFE0132400), the Shanghai Sailing Program (19YF1415300), and the China Postdoctoral Science Foundation (2018M630426).

AUTHOR CONTRIBUTIONS

D.Z. designed the experiments, supervised the projects, and contributed to the revision of this paper. M.N.K. and L.H. contributed equally to this work. They performed catalyst preparation and catalyst characterizations, prepared the figures, and co-wrote the manuscript. P.W. analyzed the experimental results. All authors discussed the results, drew conclusions, and commented on the manuscript.

DECLARATION OF INTERESTS

The authors declare no competing interests.

Received: February 21, 2020
Revised: April 26, 2020
Accepted: May 13, 2020
Published: June 26, 2020

REFERENCES

Davydov, A. (2003). Molecular Spectroscopy of Oxide Catalyst Surfaces (John Wiley & Sons Ltd), p. 124, Chapter 2.

Ding, S., Liu, F., Shi, X., Liu, K., Lian, Z., Xie, L., and He, H. (2015). Significant promotion effect of Mo additive on a Novel Ce–Zr mixed oxide catalyst for the selective catalytic reduction of NO_x with NH_3. ACS Appl. Mater. Interfaces *7*, 9497–9506.

Due-Hansen, J., Boghosian, S., Kustov, A., Fristrup, P., Tsilomelekis, G., Ståhl, K., Christensen, C.H., and Fehrmann, R. (2007). Vanadia-based SCR catalysts supported on tungstated and sulfated zirconia: influence of doping with potassium. J. Catal. *251*, 459–473.

Gao, S., Wang, P., Chen, X., Wang, H., Wu, Z., Liu, Y., and Weng, X. (2014). Enhanced alkali resistance of CeO_2/SO_4^{2-}–ZrO_2 catalyst in selective catalytic reduction of NO_x by ammonia. Catal. Commun. *43*, 223–226.

Han, L., Cai, S., Gao, M., Hasegawa, J., Wang, P., Zhang, J., Shi, L., and Zhang, D. (2019a). Selective catalytic reduction of NO_x with NH_3 by using novel catalysts: state of the art and Future prospects. Chem. Rev. *119*, 10916–10976.

Han, L., Gao, M., Feng, C., Shi, L., and Zhang, D. (2019b). Fe_2O_3–CeO_2@Al_2O_3 nanoarrays on Al-mesh as SO_2-tolerant monolith catalysts for NO_x reduction by NH_3. Environ. Sci. Technol. *53*, 5946–5956.

Han, L., Gao, M., Hasegawa, J., Li, S., Shen, Y., Li, H., Shi, L., and Zhang, D. (2019c). SO_2-tolerant selective catalytic reduction of NO_x over meso-TiO_2@Fe_2O_3@Al_2O_3 metal-based monolith catalysts. Environ. Sci. Technol. *53*, 6462–6473.

Hao, Z., Shen, Z., Li, Y., Wang, H., Zheng, L., Wang, R., Liu, G., and Zhan, S. (2019). The role of alkali metal in α-MnO_2 catalyzed ammonia-selective catalysis. Angew. Chem. Int. Ed. *58*, 6351–6356.

Hu, H., Cai, S., Li, H., Huang, L., Shi, L., and Zhang, D. (2015a). Mechanistic aspects of deNO_x processing over TiO_2 supported Co–Mn oxide catalysts: structure–activity relationships and in situ DRIFTs analysis. ACS Catal. *5*, 6069–6077.

Hu, P., Huang, Z., Gu, X., Xu, F., Gao, J., Wang, Y., Chen, Y., and Tang, X. (2015b). Alkali-resistant mechanism of a hollandite deNOx catalyst. Environ. Sci. Technol. *49*, 7042–7047.

Huang, Z., Gu, X., Wen, W., Hu, P., Makkee, M., Lin, H., Kapteijn, F., and Tang, X. (2013). A "Smart" hollandite deNO_x catalyst: self-protection against alkali poisoning. Angew. Chem. Int. Ed. *52*, 660–664.

Huang, L., Zha, K., Namuangruk, S., Junkaew, A., Zhao, X., Li, H., Shi, L., and Zhang, D. (2016). Promotional effect of the TiO_2 (001) facet in the selective catalytic reduction of NO with NH_3: in situ DRIFTS and DFT studies. Catal. Sci. Technol. *6*, 8516–8524.

Huang, L., Hu, X., Yuan, S., Li, H., Yan, T., Shi, L., and Zhang, D. (2017). Photocatalytic preparation of nanostructured MnO_2-(Co_3O_4)/TiO_2 hybrids: the formation mechanism and catalytic application in SCR deNO_x reaction. Appl. Catal. B *203*, 778–788.

Jeong, Y.E., Kumar, P.A., Huong, D.T., Ha, H.P., and Lee, K. (2017). In situ-DRIFTS study of Sb–V–CeO_2/TiO_2 catalyst under standard and fast NH_3-SCR conditions. Top. Catal. *60*, 755–762.

Li, Y., Cheng, H., Li, D., Qin, Y., Xie, Y., and Wang, S. (2008). WO_3/CeO_2-ZrO_2, a promising catalyst for selective catalytic reduction (SCR) of NO_x with NH_3 in diesel exhaust. Chem. Commun. *44*, 1470–1472.

Liu, F., and He, H. (2010). Structure−activity relationship of iron titanate catalysts in the selective catalytic reduction of NO_x with NH_3. J. Phys. Chem. C *114*, 16929–16936.

Liu, J., Meeprasert, J., Namuangruk, S., Zha, K., Li, H., Huang, L., Maitarad, P., Shi, L., and Zhang, D. (2017). Facet–activity relationship of TiO_2 in Fe_2O_3/TiO_2 canocatalysts for selective catalytic reduction of NO with NH_3: in situ DRIFTs and DFT studies. J. Phys. Chem. C *121*, 4970–4979.

Liu, N., Wang, J., Wang, F., and Liu, J. (2018). Promoting effect of tantalum and antimony additives on deNO_x performance of $Ce_3Ta_3SbO_x$ for NH_3-SCR reaction and DRIFT studies. J. Rare Earths *36*, 594–602.

Ma, L., Cheng, Y., Cavataio, G., McCabe, R.W., Fu, L., and Li, J. (2014). In situ DRIFTS and temperature-programmed technology study on NH_3-SCR of NO_x over Cu-SSZ-13 and Cu-SAPO-34 catalysts. Appl. Catal. B *156-157*, 428–437.

Marberger, A., Ferri, D., Elsener, M., and Kröcher, O. (2016). The significance of lewis acid sites for the selective catalytic reduction of nitric oxide on vanadium-based catalysts. Angew. Chem. Int. Ed. *55*, 11989–11994.

Paolucci, C., Khurana, I., Parekh, A., Li, S., Shih, A., Li, H., Di Iorio, J., Albarracin-Caballero, J., Yezerets, A., Miller, J., et al. (2017). Dynamic multinuclear sites formed by mobilized copper ions in NO_x selective catalytic reduction. Science *357*, 898–903.

Park, J.H., Pang, C., Chung, C.-H., and Bae, J.W. (2016). Methyl acetate synthesis by esterification on the modified ferrierite: correlation of acid sites measured by pyridine IR and NH_3-TPD for steady-state activity. J. Nanosci. Nanotechnol. *16*, 4626–4630.

Peng, Y., Li, J., Huang, X., Li, X., Su, W., Sun, X., Wang, D., and Hao, J. (2014). Deactivation mechanism of potassium on the V_2O_5/CeO_2 catalysts for SCR reaction: acidity, reducibility and adsorbed-NO_x. Environ. Sci. Technol. *48*, 4515–4520.

Peng, Y., Si, W., Li, X., Chen, J., Li, J., Crittenden, J., and Hao, J. (2016). Investigation of the poisoning mechanism of lead on the CeO_2–WO_3 catalyst for the NH_3–SCR reaction via in situ IR and Raman spectroscopy measurement. Environ. Sci. Technol. *50*, 9576–9582.

Putluru, S.S.R., Riisager, A., and Fehrmann, R. (2011). Alkali resistant Cu/zeolite deNO_x catalysts for flue gas cleaning in biomass fired applications. Appl. Catal. B *101*, 183–188.

Putluru, S.S.R., Kristensen, S.B., Due-Hansen, J., Riisager, A., and Fehrmann, R. (2012). Alternative alkali resistant deNO_x catalysts. Catal. Today *184*, 192–196.

Qu, W., Liu, X., Chen, J., Dong, Y., Tang, X., and Chen, Y. (2020). Single-atom catalysts reveal the dinuclear characteristic of active sites in NO selective reduction with NH_3. Nat. Commun. *11*, 1532.

Sánchez Escribano, V., Gallardo Amores, J.M., Fernández López, E., del Hoyo Martínez, C., Busca, G., and Resini, C. (2009). Surface and structural characterization of ZrO_2–CeO_2-supported molybdenum oxide catalysts. Mater. Chem. Phys. *114*, 848–853.

Sugawara, K., Nobukawa, T., Yoshida, M., Sato, Y., Okumura, K., Tomishige, K., and Kunimori, K. (2007). The importance of Fe loading on the N_2O reduction with NH_3 over Fe-MFI: effect of acid site formation on Fe species. Appl. Catal. B *69*, 154–163.

Wang, P., Wang, H., Chen, X., Liu, Y., Weng, X., and Wu, Z. (2015). Novel SCR catalyst with superior alkaline resistance performance: enhanced self-protection originated from modifying protonated titanate nanotubes. J. Mater. Chem. A *3*, 680–690.

Wang, P., Sun, H., Quan, X., and Chen, S. (2016). Enhanced catalytic activity over MIL-100(Fe) loaded ceria catalysts for the selective catalytic reduction of NO_x with NH_3 at low temperature. J. Hazard. Mater. *301*, 512–521.

Wang, X., Cong, Q., Chen, L., Shi, Y., Shi, Y., Li, S., and Li, W. (2019). The alkali resistance of CuNbTi catalyst for selective reduction of NO by NH_3: a comparative investigation with VWTi catalyst. Appl. Catal. B *246*, 166–179.

Wei, L., Cui, S., Guo, H., Ma, X., and Zhang, L. (2016). DRIFT and DFT study of cerium addition on SO_2 of Manganese-based Catalysts for low temperature SCR. J. Mol. Catal. A *421*, 102–108.

Wei, L., Cui, S., Guo, H., and Zhang, L. (2018). The effect of alkali metal over Mn/TiO_2 for low-temperature SCR of NO with NH_3 through DRIFT and DFT. Comput. Mater. Sci. *144*, 216–222.

Weng, X., Dai, X., Zeng, Q., Liu, Y., and Wu, Z. (2016). DRIFT studies on promotion mechanism of $H_3PW_{12}O_{40}$ in selective catalytic reduction of NO with NH_3. J. Colloid. Interface Sci. *461*, 9–14.

Yu, Y., Wang, J., Chen, J., Meng, X., Chen, Y., and He, C. (2014). Promotive effect of SO_2 on the activity of a deactivated commercial selective catalytic reduction catalyst: an in situ DRIFT study. Ind. Eng. Chem. Res. *53*, 16229–16234.

Zhang, H., Zou, Y., and Peng, Y. (2017). Influence of sulfation on CeO_2-ZrO_2 catalysts for NO reduction with NH_3. Chin. J. Catal. *38*, 160–167.

Zhang, Y., Yue, X., Huang, T., Shen, K., and Lu, B. (2018). In situ DRIFTS studies of NH_3-SCR mechanism over V_2O_5-CeO_2/TiO_2-ZrO_2 catalysts for selective catalytic reduction of NO_x. Materials *11*, 1307.

Zheng, L., Zhou, M., Huang, Z., Chen, Y., Gao, J., Ma, Z., Chen, J., and Tang, X. (2016). Self-protection mechanism of hexagonal WO_3–based deNO_x catalysts against alkali poisoning. Environ. Sci. Technol. *50*, 11951–11956.

iScience, Volume *23*

Supplemental Information

Tailored Alkali Resistance of $DeNO_x$ Catalysts by Improving Redox Properties and Activating Adsorbed Reactive Species

Mehak Nawaz Khan, Lupeng Han, Penglu Wang, and Dengsong Zhang

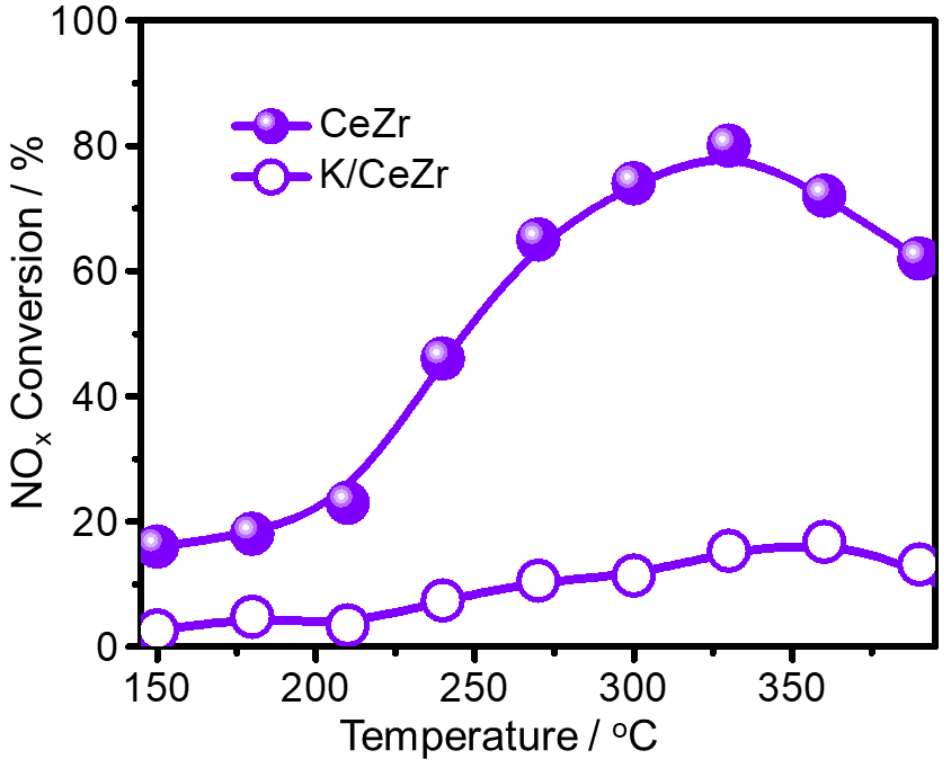

Figure S1. NO conversion during the SCR reaction over CeZr and K-poisoned CeZr catalysts. Reaction conditions: 500 ppm NO, 500 ppm NH_3, 5 vol % O_2, N_2 as the balance gas, and GHSV of 100000 h^{-1}, Related to Figure 1.

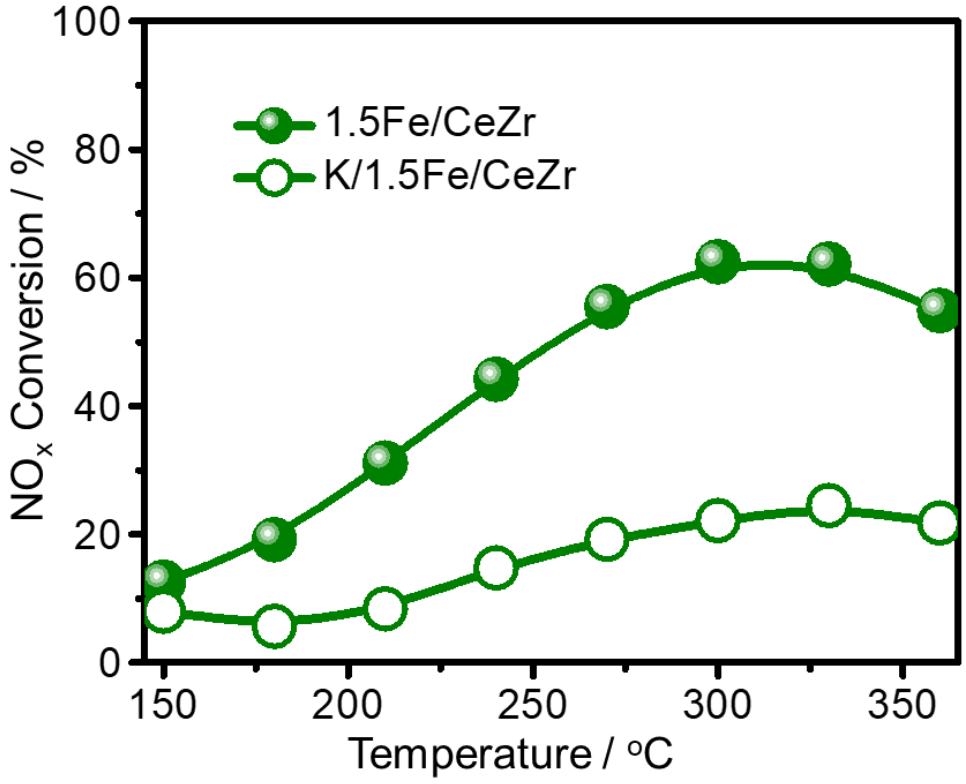

Figure S2. NO conversion during the SCR reaction over 1.5Fe/CeZr and K-poisoned 1.5Fe/CeZr catalysts. Reaction conditions: 500 ppm NO, 500 ppm NH_3, 5 vol % O_2, N_2 as the balance gas, and GHSV of 100000 h^{-1}, Related to Figure 1.

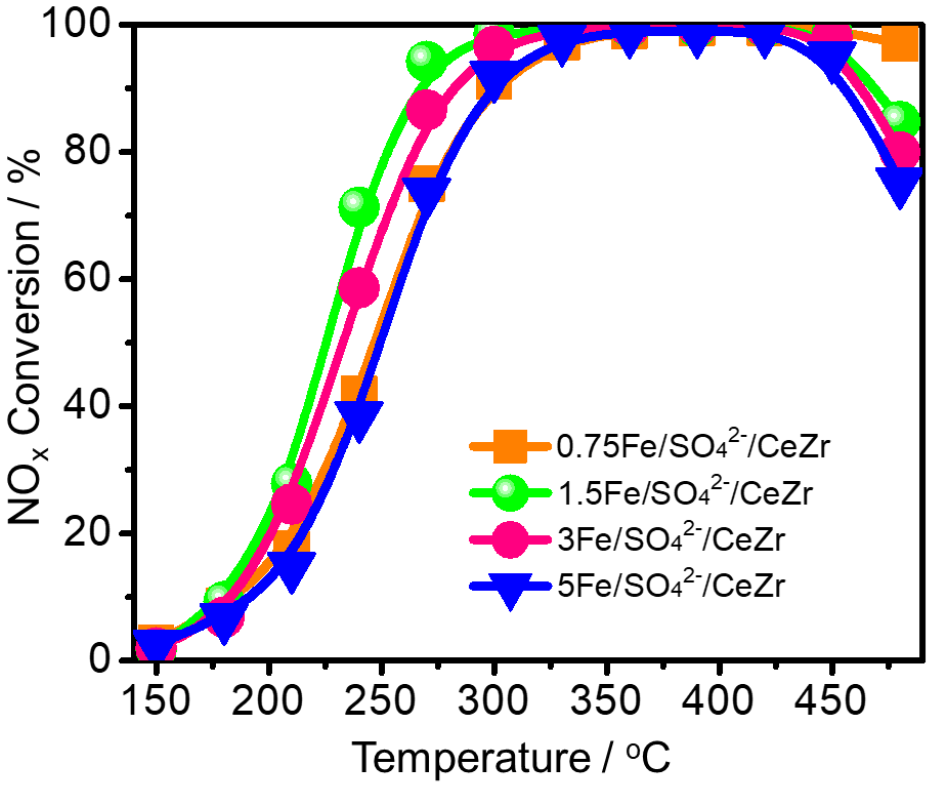

Figure S3. NO conversion during the SCR reaction over various catalysts. Reaction conditions: 500 ppm NO, 500 ppm NH_3, 5 vol % O_2, N_2 as the balance gas, and GHSV of 100000 h^{-1}, Related to Figure 1.

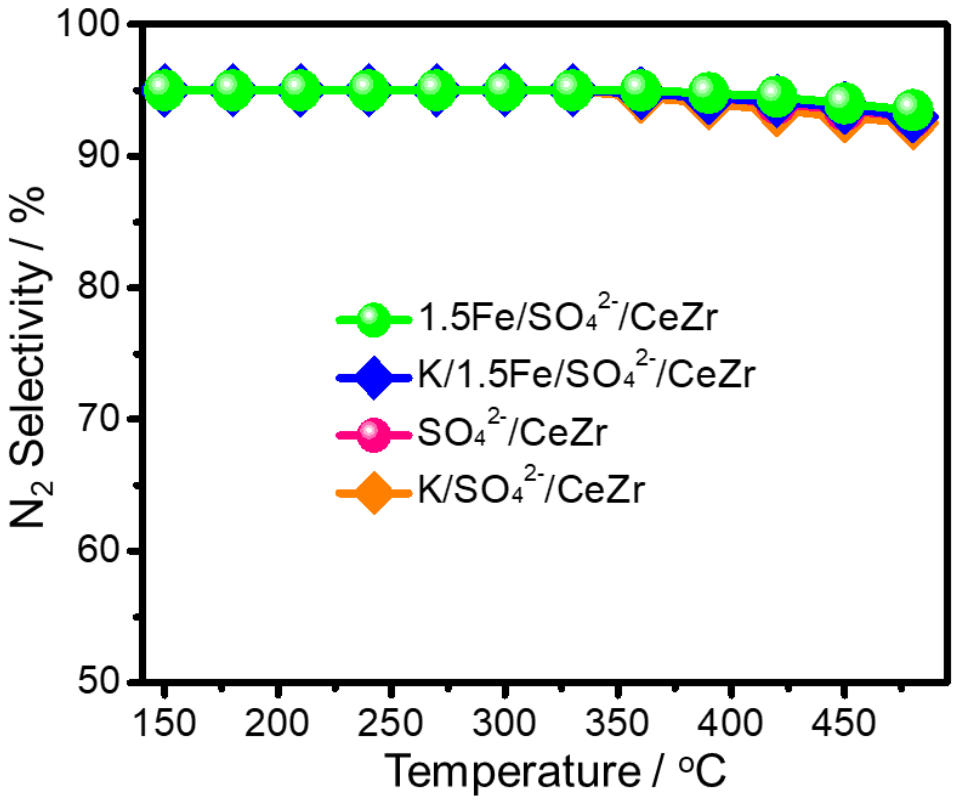

Figure S4. N_2 selectivity during the SCR reaction over fresh and K-poisoned SO_4^{2-}/CeZr and Fe/SO_4^{2-}/CeZr catalysts. Reaction conditions: 500 ppm NO, 500 ppm NH_3, 5 vol % O_2, N_2 as the balance gas, and GHSV of 100000 h^{-1}, Related to Figure 1.

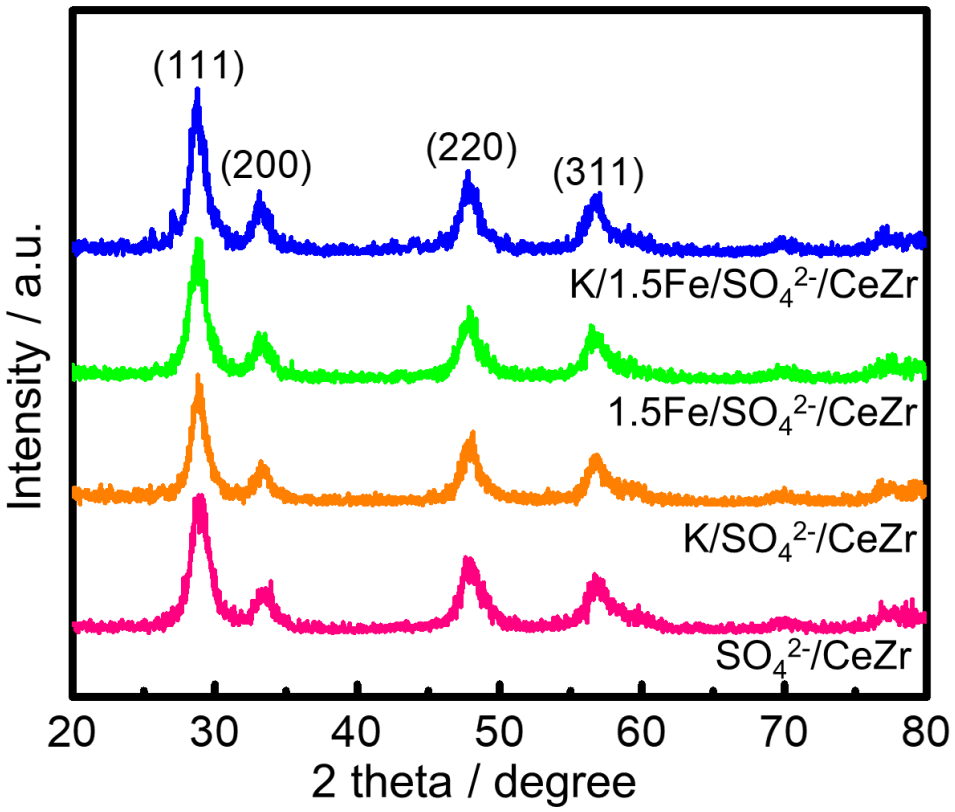

Figure S5. XRD patterns of fresh and K-poisoned SO_4^{2-}/CeZr and 1.5Fe/SO_4^{2-}/CeZr catalysts, Related to Figure 2.

XRD patterns of all catalysts show the cubic fluorite phase of CeO_2 (Zhang et al., 2017). No characteristic diffraction peak of ZrO_2 are observed likely due to the formation of Ce-Zr solid solution.

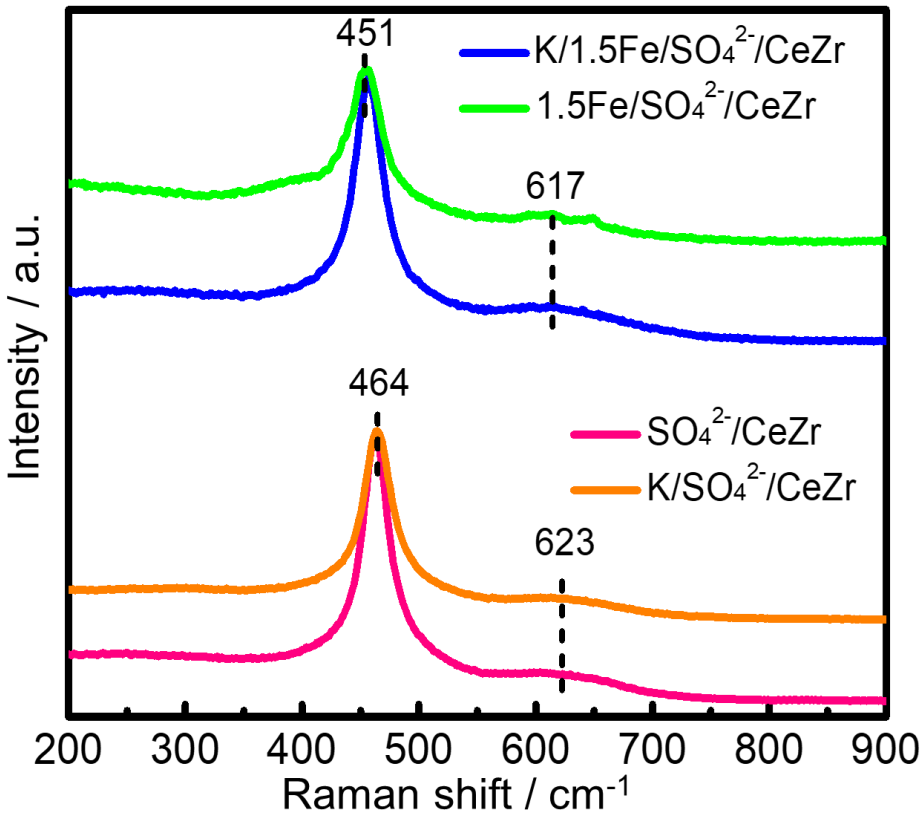

Figure S6. Raman spectra of fresh and K-poisoned SO_4^{2-}/CeZr and 1.5Fe/SO_4^{2-}/CeZr catalysts, Related to Figure 2.

All catalysts show two bands around 460 cm^{-1} and 620 cm^{-1}. The band around 460 cm^{-1} was attributed to the F2g vibration of the fluorite-type lattice, which is a symmetric breathing mode of the oxygen atoms around cerium ions. The band near 620 cm^{-1} is likely attributed to a nondegenerate longitudinal optical mode of ceria (Reddy et al., 2003). No Zr-related bands are observed due to the formation of Ce-Zr solid solution.

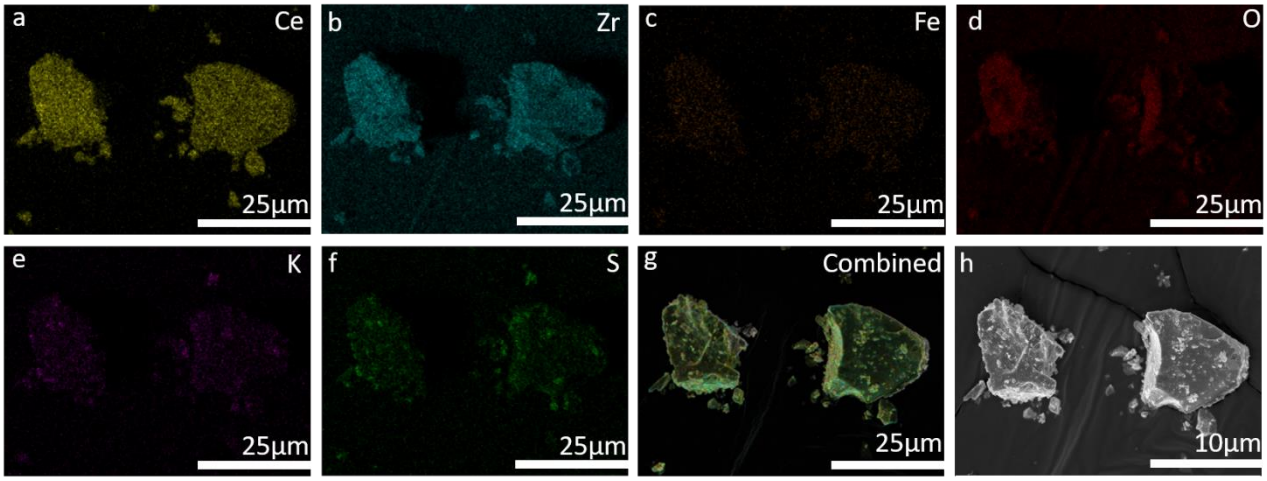

Figure S7. SEM elemental mappings of the representative K/1.5Fe@SO_4^{2-}@CeZr catalyst, Related to Figure 2.

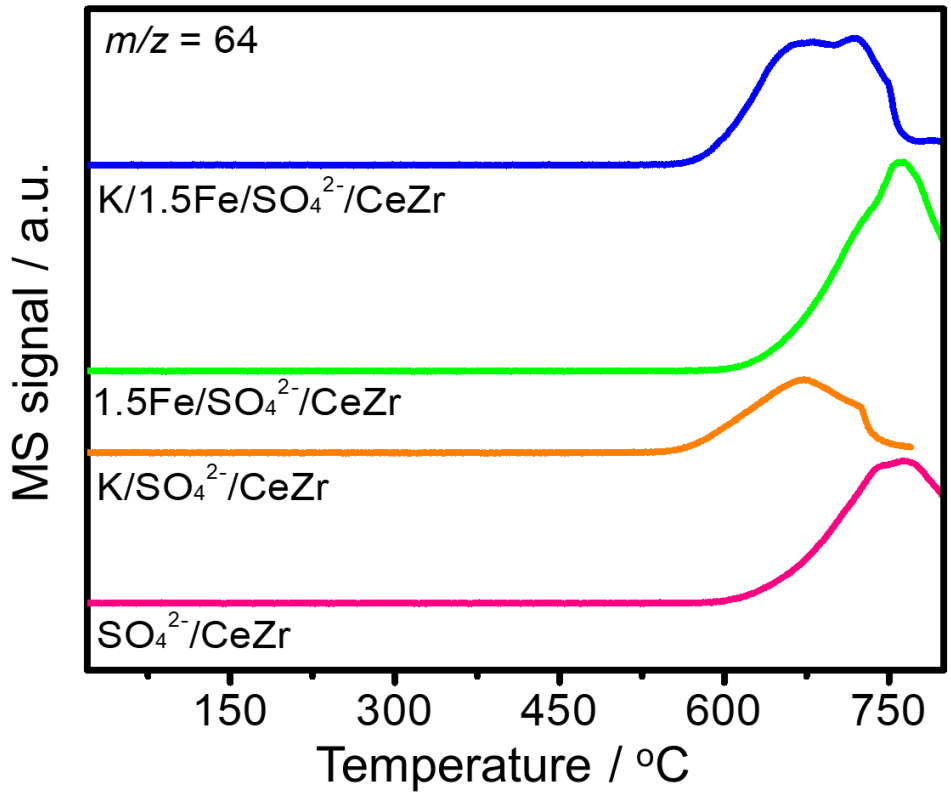

Figure S8. The profiles of SO_2 (*m/z*=64) detected from the NH_3-TPD-MS for different catalysts, Related to Figure 2.

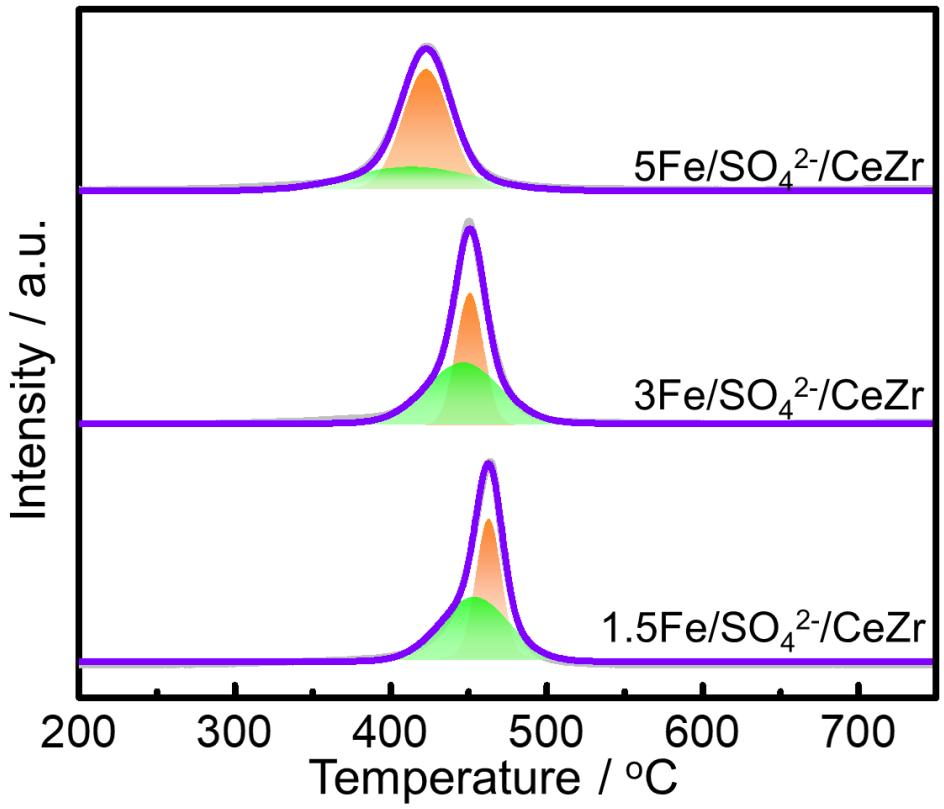

Figure S9. H_2-TPR profiles of 1.5Fe/SO_4^{2-}/CeZr, 3Fe/SO_4^{2-}/CeZr and 5Fe/SO_4^{2-}/CeZr catalysts, Related to Figure 2.

With increasing the amount of Fe, the reduction peaks of further shift to lower temperatures, but the FeO_x reduction peak (low-temperature peak) does not increase, indicating more FeO_x interacted with CeO_x species and the reduction peak of FeO_x may overlap with that of CeO_x. This results further evidence the existence of strong interaction between FeO_x and CeO_x.

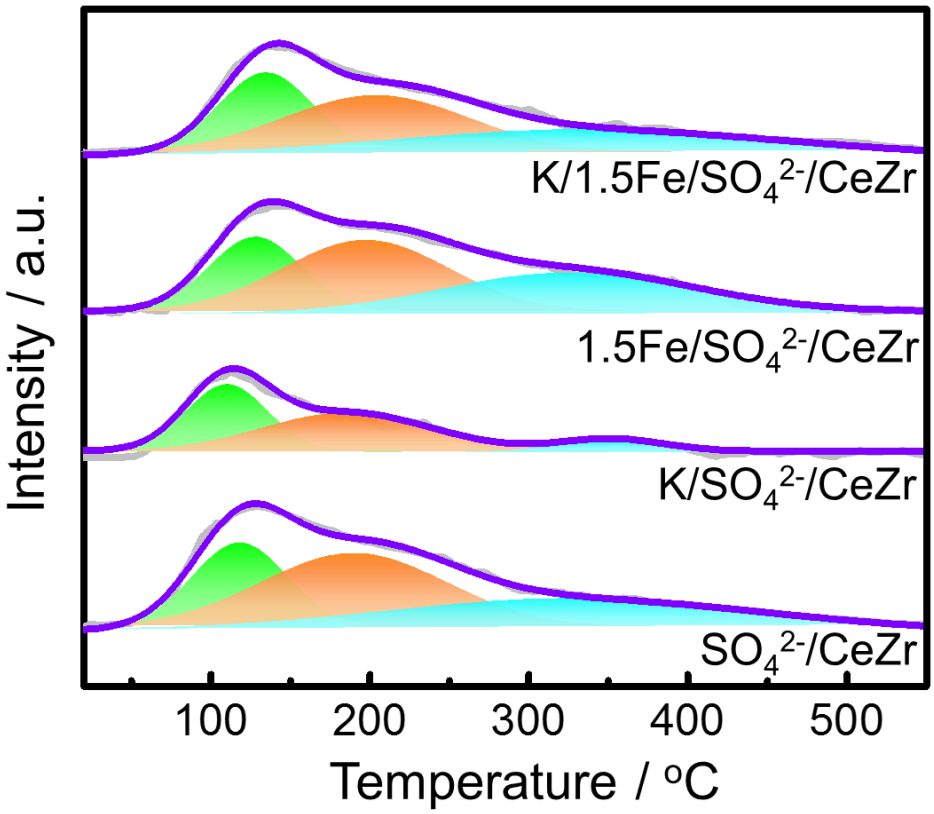

Figure S10. O_2-TPD profiles of different catalysts, Related to Figure 2.

All catalysts show three desorption peaks of O_2, which can be assigned to physically adsorbed oxygen O_2, chemically adsorbed oxygen O^{2-} and chemically adsorbed oxygen O^- species (Li et al., 2011).

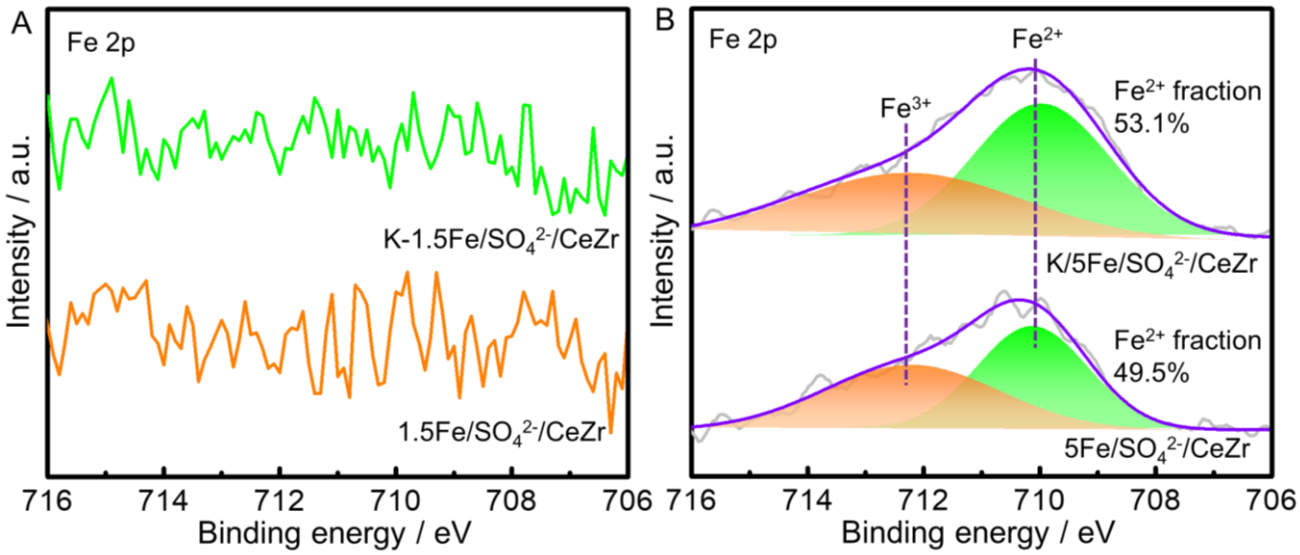

Figure S11. (A) The XPS spectra of 1.5Fe/SO_4^{2-}/CeZr and K/1.5Fe/SO_4^{2-}/CeZr; (B) The XPS spectra of 5Fe/SO_4^{2-}/CeZr and K/5Fe/SO_4^{2-}/CeZr, Related to Figure 2.

The Fe 2p spectra of catalysts are fitted into two peaks, which correspond to Fe^{2+} (712.2 eV) and Fe^{3+} (709.9 eV), respectively (France et al., 2017).

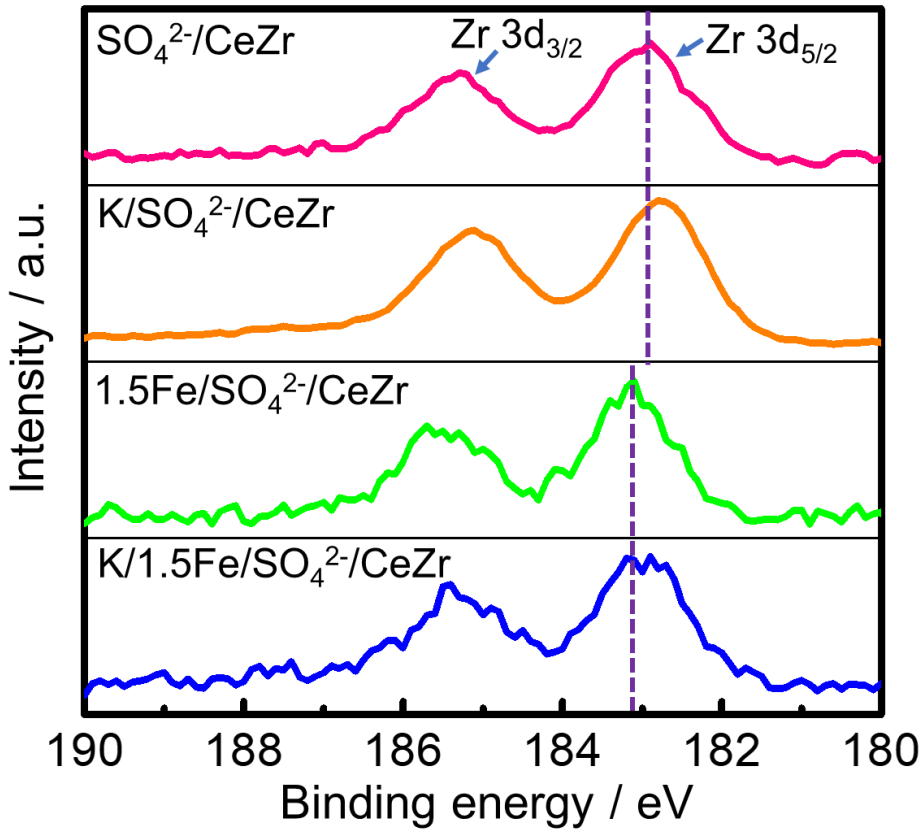

Figure S12. XPS spectra of Zr 3d over different catalysts, Related to Figure 2.

The Zr 3d spectra show Zr $3d_{5/2}$ with binding energy around 183 eV, which corresponds to the Zr^{4+} state (Sun et al., 2018). Fe decorated SO_4^{2-}/CeZr has higher binding energy of Zr $3d_{5/2}$ than SO_4^{2-} /CeZr, indicating Fe likely gets electron from Zr due to the strong interaction between Fe and Zr. After K poisoning, the Zr $3d_{5/2}$ binding energy of both catalysts shifts to a lower value, implying K as an electron donating promoter reduces the valence of Ce species.

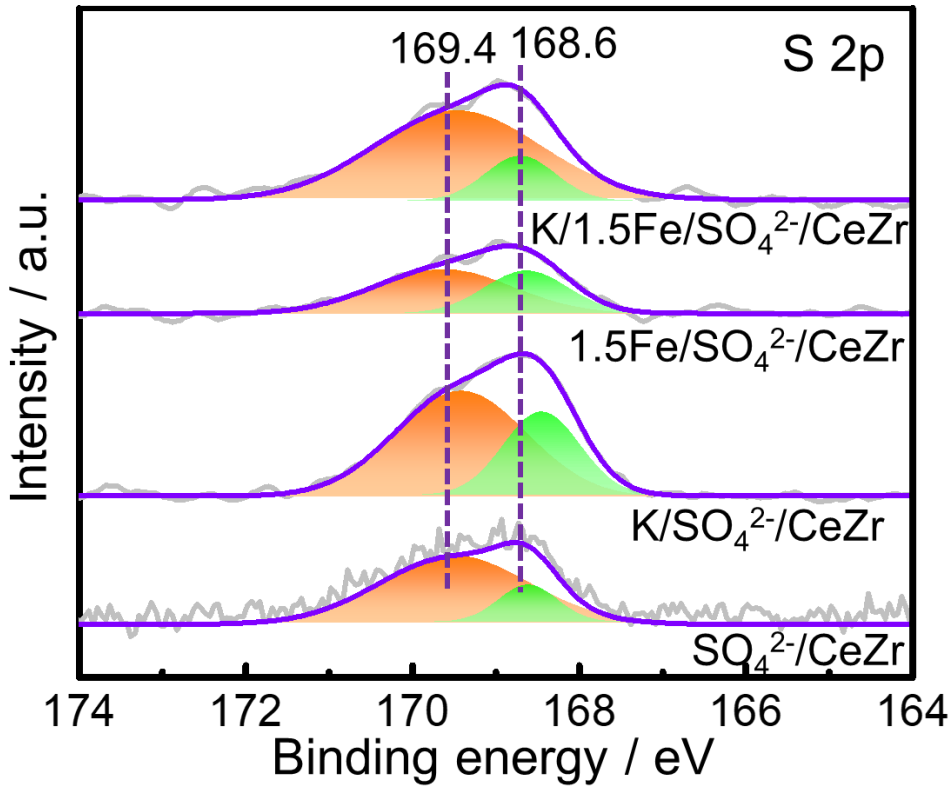

Figure S13. XPS spectra of S 2p over different catalysts, Related to Figure 2.

The S 2p spectra of catalysts are fitted into two peaks at 169.4 eV and 168.6 eV, which are both attributed to SO_4^{2-} species for S $2p_{1/2}$ and S $2p_{3/2}$, respectively (Zhao et al., 2019).

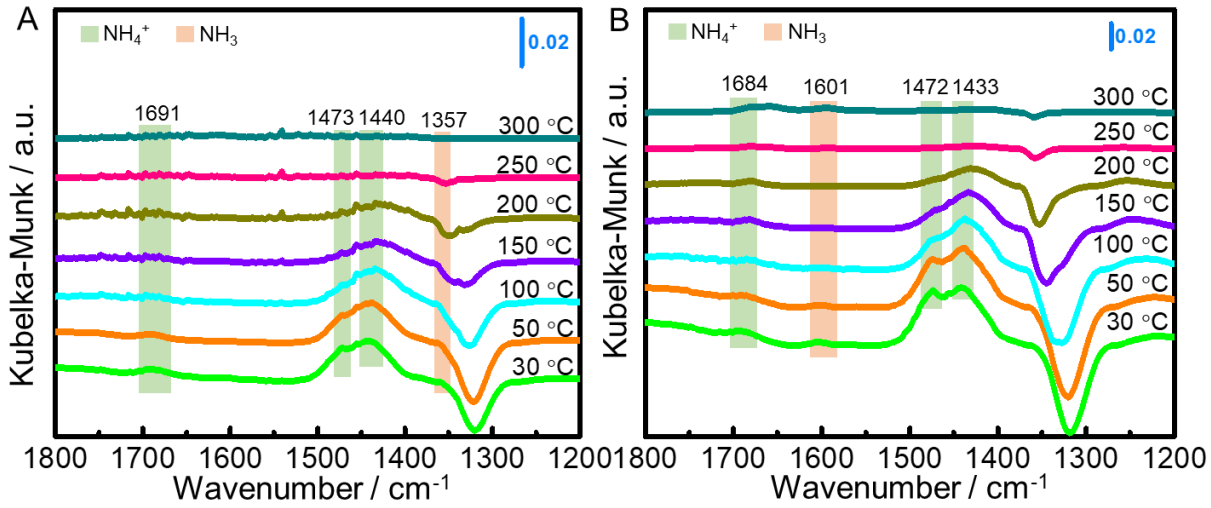

Figure S14. *In situ* DRIFTs of NH_3 desorption over (A) SO_4^{2-}/CeZr and (B) 1.5Fe/SO_4^{2-}/CeZr catalysts after exposure to a flow of 500 ppm NH_3 for 1 h at 30 °C, Related to Figure 3.

For SO_4^{2-}/CeZr catalysts, NH_4^+ (1691, 1473,1440 cm^{-1}) (Huang et al., 2017; Huang et al., 2016; Wei et al., 2016) and NH_3 (1357 cm^{-1}) (Zhang et al., 2018) species appear SO_4^{2-}/CeZr catalysts after NH_3 adsorption, and gradually reduce with the increased temperature and only few NH_4^+ species reserve at 250 ºC and 300 ºC. Similarly, NH_4^+ (1684,1472,1433 cm^{-1}) (Liang et al., 2016) and NH_3 (1601 cm^{-1}) (Zhang et al., 2018) adsorb on 1.5Fe/SO_4^{2-}/CeZr catalysts and gradually reduce with the increased temperature and few NH_4^+ and NH_3 species remain above 250 ºC. These results indicate that adsorbed NH_x species are not stable above 250 ºC.

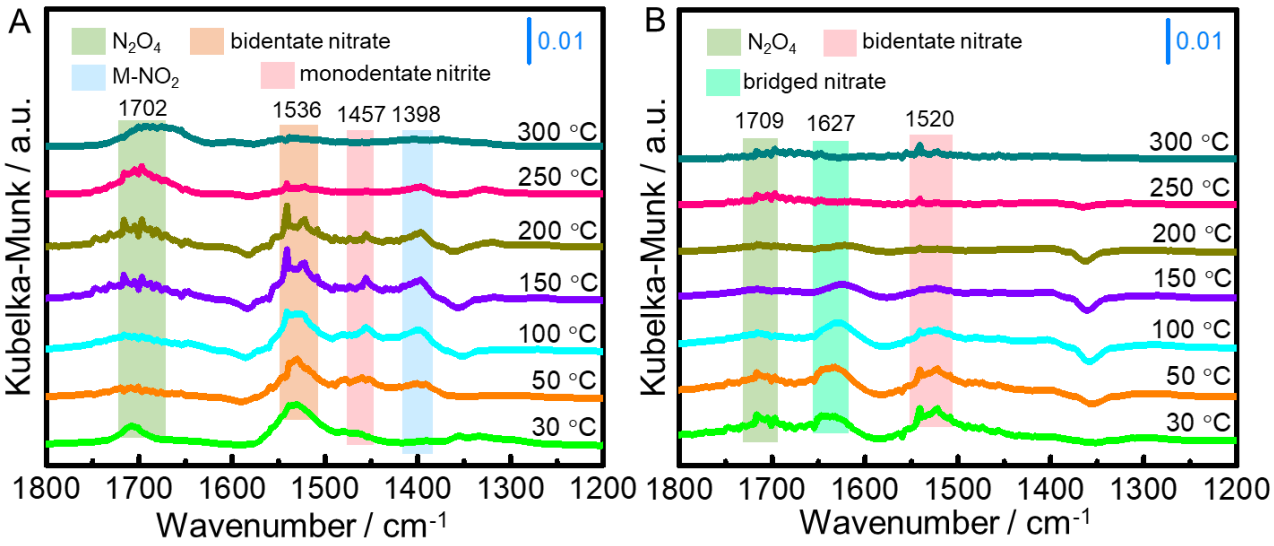

Figure S15. *In situ* DRIFTs of NO+O_2 desorption over (A) SO_4^{2-}/CeZr and (B) 1.5Fe/SO_4^{2-}/CeZr catalysts after exposure to a flow of 500 ppm NO + 5% O_2 for 1 h at 30 °C, Related to Figure 3.

For SO_4^{2-}/CeZr, N_2O_4 (1702 cm^{-1}) (Huang et al., 2017), bidentate nitrate (1536 cm^{-1}) (Hu et al., 2016), monodentate nitrite (1457 cm^{-1}) (Liu et al., 2018a), and metal-NO_2 (1398 cm^{-1}) (Davydov, 2003) species appear after NO+O_2 adsorption. These species gradually reduce with increasing the temperature. Similarly, N_2O_4 (1709 cm^{-1}), bridged nitrate species (1627 cm^{-1}) (Baltrusaitis et al., 2007) and bidentate nitrate (1520 cm^{-1}) (Davydov, 2003) species adsorbed on 1.5Fe/SO_4^{2-}/CeZr and gradually reduce with increasing the temperature. It is notable that nitrate species on 1.5Fe/SO_4^{2-}/CeZr desorb more easily than on SO_4^{2-}/CeZr, indicating the weaker adsorbed strength of the former one. This also implies the high reactivity of nitrate species on 1.5Fe/SO_4^{2-}/CeZr.

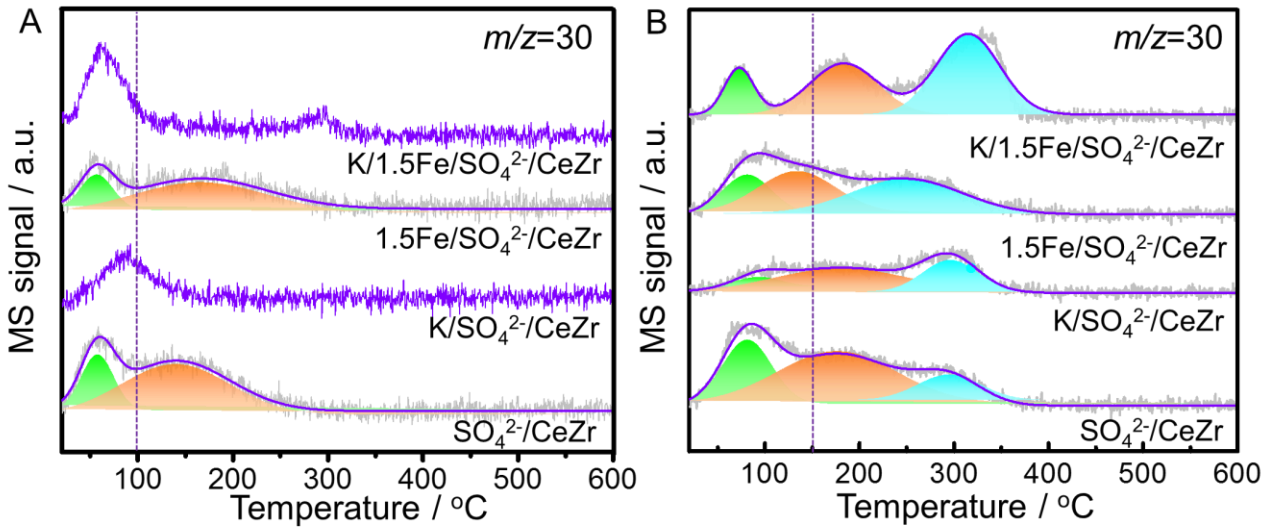

Figure S16. (A) NO-TPD-MS and (B) NO+O_2-TPD-MS profiles of fresh and K-poisoned SO_4^{2-}/CeZr and 1.5Fe/SO_4^{2-}/CeZr catalysts. NO signal (*m/z*=30) was detected during the NO_x-TPD process, Related to Figure 3.

For the NO-TPD-MS, fresh SO_4^{2-}/CeZr and 1.5Fe/SO_4^{2-}/CeZr catalysts show two NO_x desorption peaks, and the one below 100 °C is attributed to the physically adsorbed NO and the one above 100 °C is related to chemically adsorbed NO_x with higher thermal stability. The chemically adsorbed NO_x obviously decreases for both K-poisoned SO_4^{2-}/CeZr and 1.5Fe/SO_4^{2-}/CeZr catalysts. It is notable that K/1.5Fe/SO_4^{2-}/CeZr shows one NO_x desorption peak at 300 °C but no NO_x desorption peak is found over K/SO_4^{2-}/CeZr above 200 °C, which will influence the formation of active nitrate species when O_2 exists.

For the NO+O_2-TPD-MS, the NO_x desorption peaks below 150 °C could be attributed to the physically adsorbed NO_x and the peaks above 150 °C were due to the chemically adsorbed monodentate nitrate, bridging nitrate or bidentate nitrate species (Lian et al., 2014). The adsorbed nitrate species over SO_4^{2-}/CeZr decreases after K-poisoning while those over 1.5Fe/SO_4^{2-}/CeZr increases after K-poisoning. This indicates that Fe decoration helps to improve the formation of nitrite species likely due to the improvement of redox properties after K-poisoning.

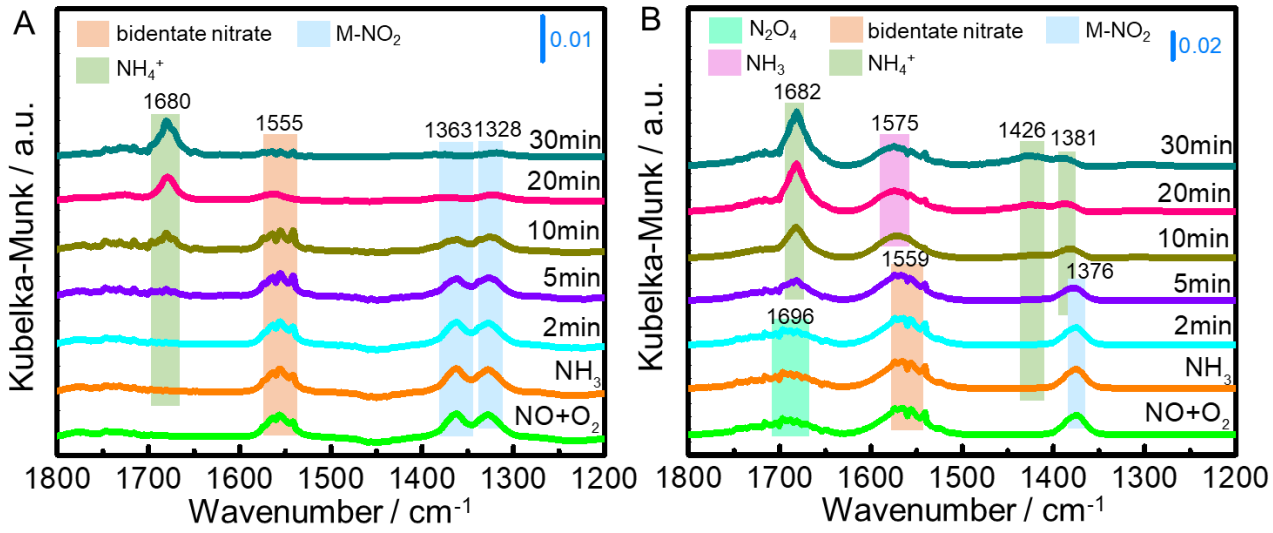

Figure S17. *In situ* DRIFTs of the transient reactions between NH_3 and pre-adsorbed $NO+O_2$ over (A) SO_4^{2-}/CeZr and (B) 1.5Fe/SO_4^{2-}/CeZr catalysts at 250 °C as a function of time, Related to Figure 4.

For SO_4^{2-}/CeZr, bidentate nitrates (1555 cm^{-1}) (Hu et al., 2015) and M-NO_2 (1363 and 1328 cm^{-1}) (Davydov, 2003) species appear after the adsorption of $NO+O_2$, and these species gradually decrease and vanish after introducing NH_3 for 30 min. Meanwhile, NH_4^+ species (1680 cm^{-1}) (Liang et al., 2016) increase with continuous introduction of NH_3. For 1.5Fe/SO_4^{2-}/CeZr catalysts, N_2O_4 (1696 cm^{-1}) (Huang et al., 2017), bidentate nitrates (1559 cm^{-1}) and M-NO_2 (1376 cm^{-1}) (Davydov, 2003) species appear after the adsorption of $NO+O_2$, and these species gradually decrease within 5 min after introducing NH_3. Meanwhile, NH_4^+ species (1682, 1426 and 1381 cm^{-1}) (Ma et al., 2014; Weng et al., 2016) and NH_3 (1575 cm^{-1}) (Yan et al., 2017) species gradually emerge. These results indicate that the adsorbed nitrate species are reactive over both catalysts, which can react with adsorbed NH_4^+ or NH_3 species. Moreover, the reactivity of nitrate species over 1.5Fe/SO_4^{2-}/CeZr is faster than that over SO_4^{2-}/CeZr.

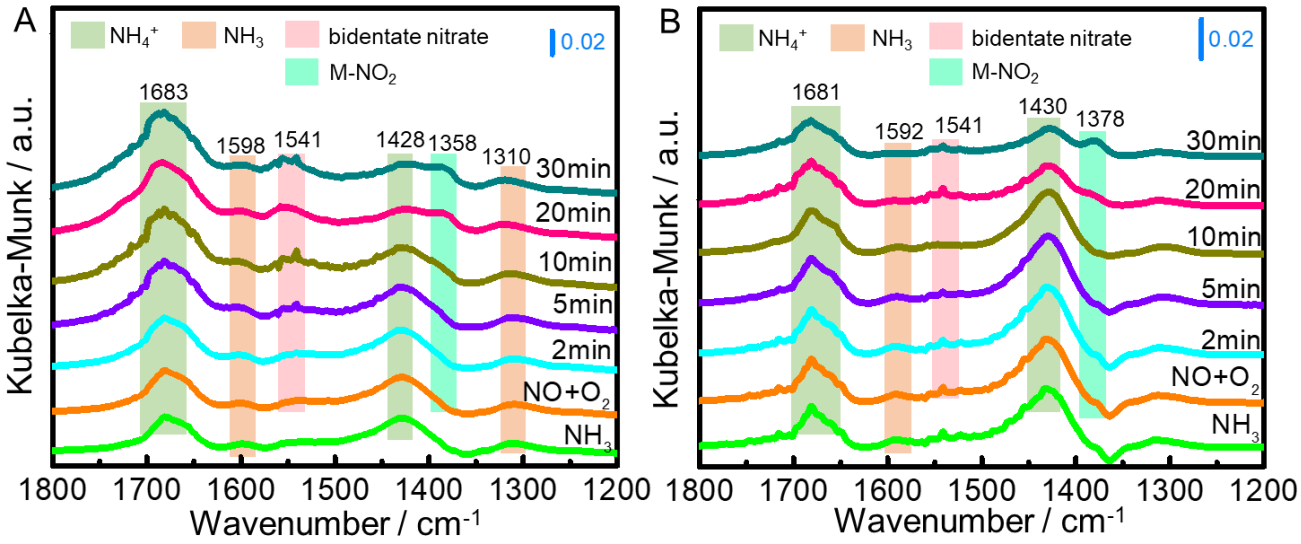

Figure S18. *In situ* DRIFTs of the transient reactions between $NO+O_2$ and pre-adsorbed NH_3 over (A) SO_4^{2-}/CeZr and (B) 1.5Fe/SO_4^{2-}/CeZr catalysts at 250 °C as a function of time, Related to Figure 4.

For SO_4^{2-}/CeZr catalysts, NH_4^+ (1683 and 1428 cm^{-1}) (Chen et al., 2016; Liu et al., 2014) and NH_3 (1598 and 1310 cm^{-1}) (Hu et al., 2015; Liu et al., 2018b) species appear after the adsorption of NH_3. The NH_3 species keep unchanged and NH_4^+ species (1428 cm^{-1}) decrease slowly with introducing $NO+O_2$. Meanwhile, the bidentate nitrate (1541 cm^{-1}) (Hu et al., 2015) and M=NO_2 (1358 cm^{-1}) (Davydov, 2003) species gradually emerge with continuous introduction of $NO+O_2$. 1.5Fe/SO_4^{2-}/CeZr catalysts show the adsorbed NH_4^+ (1681 and 1430 cm^{-1}) and NH_3 (1592 cm^{-1}) species, in which the reactivity of NH_3 (1592 cm^{-1}) and NH_4^+ species (1430 cm^{-1}) are faster than those on SO_4^{2-}/CeZr. Meanwhile, bidentate nitrate (1541 cm^{-1}) and M=NO_2 (1378 cm^{-1}) species when introducing $NO+O_2$.

Table S1. Textural properties of fresh and K-poisoned SO_4^{2-}/CeZr and 1.5Fe/SO_4^{2-}/CeZr catalysts, Related to Figure 2.

Catalyst	Surface Area (m^2 g^{-1})	Pore Volume (cm^3 g^{-1})	Average Pore diameter (nm)
1.5Fe/SO_4^{2-}/CeZr	44.42	0.055	3.788
K/1.5Fe/SO_4^{2-}/CeZr	66.29	0.070	3.708
SO_4^{2-}/CeZr	60.06	0.064	3.572
K/SO_4^{2-}/CeZr	70.37	0.070	3.497

The Brunauer–Emmett–Teller (BET) surface area of SO_4^{2-}/CeZr and Fe/SO_4^{2-}/CeZr after K-poisoning both increases to some extent likely due to the contribution of K_2O nanoparticle on catalyst surface. The pore volume increases and the pore size decreases a little for both K-poisoned SO_4^{2-}/CeZr and Fe/SO_4^{2-}/CeZr because of the formation of micropore resulting from K_2O coverage.

Transparent Methods

Catalyst Preparation

CeZr mixed oxides were prepared by a co-precipitation method. Firstly, 3.25 g of $Ce(NO_3)_3 \cdot 6H_2O$ and 1.07 g of $ZrOCl_2 \cdot 8H_2O$ were dissolution in 100 mL of deionized water. Then ammonia solution was added till the pH reached to 10 and stirred the solution for 1h and then filtered and washed till pH became 7. The precipitate was then dried at 60 ^oC for 18 h and calcinated at 500 ^oC for 2 h.

SO_4^{2-}/CeZr was prepared by pretreating CeZr mixed oxides with H_2SO_4. 2 g of CeZr oxide powder was stirred in 0.5 M H_2SO_4 solution for 3 h and then filtered and dried for 12 h at 60 ^oC. Via analyzing the atom ratio from XPS results of SO_4^{2-}/CeZr, the molar ratio of SO_4^{2-}/Ce/Zr is 1/2/1.

xFe/SO_4^{2-}/CeZr was prepared by a wet impregnation method by dissolving x wt% of $Fe(NO_3)_3 \cdot 9H_2O$ (x= 0.75, 1.5, 3, 5 wt%) in 20 ml of deionized water and then 2 g of SO_4^{2-}/CeZr was added. The catalyst was then dried at 60 ^oC and calcined for 500 ^oC for 2 h.

1 wt% of K_2O poisoned catalysts were prepared by a wet impregnation method. SO_4^{2-}/CeZr and xFe/SO_4^{2-}/CeZr were impregnated with a specific amount of potassium nitrate aqueous solutions followed by drying at 60 ^oC and then calcination at 500 ^oC for 2 h. The catalysts are named as K-SO_4^{2-}/CeZr and K-xFe/SO_4^{2-}/CeZr, respectively.

Characterization

The X-ray diffraction (XRD) experiments were carried out on a Rigaku D/MAS-RB X-ray diffractometer with Cu Kα (40 kV, 40 mA) radiation, and the XRD patterns were recorded in the 2θ range of 10° to 90° with a scan rate of 8 °/min.

The Raman spectra were recorded on the LabRAM HR Evolution. The Raman spectra were acquired in the range of 100~900cm^{-1} using a laser with a wavelength of 532 nm and the spectral resolution employed was 4 cm^{-1}.

The scanning electron microscope mapping was conducted on the scanning electron microscope (ZEISS SIGMA300) with an energy dispersive detector (Oxford AZtecX-MaxN 50).

The nitrogen adsorption-desorption isotherm of the samples was measured at -196 °C using an automatic surface and pore size analyzer (Autosorb-IQ2, Quantachrome Corporation)

The acid mount of the catalysts was measured by ammonia temperature-programmed desorption-mass spectrum (NH_3-TPD-MS) using a chemisorption analyzer (TP-5080, Xianquan Industrial and Trading Co., Ltd) and an online mass spectrometer (OMNISTAR, Pfeiffer). Prior to the TPD experiments, 100 mg catalysts were outgassed under He protection (30 ml/min) at 300 °C for 30 min and then cooled to room temperature. Samples were exposed to 10% NH_3/N_2 for one hour at room temperature, the physical adsorption of ammonia was removed by He purging for 1 h at the same temperature. Finally, the temperature was raised to 800 °C with a ramping rate of 10 °C/min. The acid amount was quantitated based on the intensity of desorbed NH_3 signal (*m/z*=17) from NH_3-TPD-MS and the pulse of specific amounts of NH_3.

The X-ray photoelectron spectroscopy (XPS) systems (PHI-5300) 48 with Mg-Kα radiation were used to detect the surface atomic valence. The binding energies Ce and O were referenced to the adventitious C 1s line at 284.6 eV and the peaks were fitted by Avantage Software.

The reducibility of catalysts was measured by hydrogen temperature-programmed reduction (H_2-TPR) by using Micromeritics AutoChem II Chemisorption Analyzer, 2920.

O_2-TPD, NO-TPD and NO+O_2-TPD were measured by a chemisorption analyzer (TP-5080, Xianquan Industrial and Trading Co., Ltd) and an online mass spectrometer (OMNISTAR, Pfeiffer). Prior to the TPD experiments, 100 mg catalysts were outgassed under He protection (30 ml/min) at 300 °C for 30 min and then cooled to room temperature. Samples were exposed to 5% O_2/N_2, 500 ppm NO/N_2 or 5% O_2/N_2 + 500 ppm NO/N_2 for one hour at room temperature, the physical adsorption of ammonia was removed by He purging for 1 h at the same temperature. Finally, the temperature was raised to 800 °C with a ramping rate of 10 °C/min.

In situ diffuse reflectance infrared Fourier transform spectroscopy (*In situ* DRIFTS) experiments was carried out on a Nicolet 6700 spectrometer equipped with a Harrick Scientific DRIFTs cell and with a liquid nitrogen cooled mercury cadmium telluride (MCT) detector. The DRIFTs spectra were collected in the range of 1000-2000 cm^{-1} in Kubelka-Munk format, accumulating scans at 4 cm^{-1} resolution. Prior to each test, each sample was pretreated at 300 °C for 30 min under a 50 mL/min N_2 flow. The background spectrum at the desired temperature is collected after pretreatment, which be deducted from the sample spectra for each measurement. For the transient reactions, the catalysts were exposed to 500 ppm of NH_3 (or NO+O_2) at 250 °C for the adsorption. One hour later, the samples were switched to a flow of NO+O_2 (or NH_3), and meanwhile the reaction proceeded with time recorded. The test conditions: NO 500ppm, NH_3 500ppm, O_2 5 vol%, N_2 as the carrier gas.

Reactivity Tests

The SCR activity was conducted by using 0.3 mL of catalysts of 40-60 mesh. The condition of the gases for the reaction was adjusted as 500 ppm NO, 500 ppm NH_3, 5 vol% O_2, and N_2 as a balance gas where VM 4000 flue gas analyzer was used for the analysis of NO_x concentration. The N_2 selectivity was measured by using FTIR, Antairs by Thermo Fisher. The sum of all the gases rate of flow was 500 mL/min and gas hourly space velocity (GHSV) was 100000 h^{-1}. The NO conversion percentage, N_2 selectivity and GHSV was calculated by using the following formula:

$$\text{NO conversion (\%)} = \frac{[NO]_{in} - [NO]_{out}}{[NO]_{in}} \times 100\ \%$$

$$N_2\ \text{selectivity (\%)} = \left(1 - \frac{2[N_2O]_{out}}{[NO_x]_{in} + [NH_3]_{in} - [NO_x]_{out} - [NH_3]_{out}}\right) \times 100\ \%$$

Where NO_x stood for the total concentration of NO and NO_2. $[NO]_{in}$, $[NO]_{out}$, $[N_2O]_{out}$, $[NO_x]_{in}$, $[NO_x]_{out}$, $[NH_3]_{in}$, and $[NH_3]_{out}$ indicated the corresponding the inlet and outlet gas concentrations, respectively.

The GHSV was obtained by the following formula:

$$\text{GHSV} = \frac{q_v}{\pi h r^2}$$

q_v corresponded to the total flow rate; h meant the height of the catalyst in the reactor; and r represented the inner radius of the reactor.

REFERENCES

Baltrusaitis, J., Schuttlefield, J., Jensen, J.H., and Grassian, V.H. (2007). FTIR spectroscopy combined with quantum chemical calculations to investigate adsorbed nitrate on aluminium oxide surfaces in the presence and absence of co-adsorbed water. Phys. Chem. Chem. Phys. *9*, 4970-4980.

Chen, Q., Guo, R., Wang, Q., Pan, W., Yang, N., Lu, C., and Wang, S. (2016). The promotion effect of Co doping on the K resistance of Mn/TiO_2 catalyst for NH_3-SCR of NO. J. Taiwan Inst. Chem. E. *64*, 116-123.

Davydov, A. (2003). Molecular spectroscopy of oxide catalyst surfaces. John Wiley & Sons Ltd *Chapter 2*, pp. 124.

France, L.J., Yang, Q., Li, W., Chen, Z., Guang, J., Guo, D., Wang, L., and Li, X. (2017). Ceria modified $FeMnO_x$-Enhanced performance and sulphur resistance for low-temperature SCR of NO_x. Appl. Catal. B. *206*, 203-215.

Hu, H., Cai, S., Li, H., Huang, L., Shi, L., and Zhang, D. (2015). In situ DRIFTs investigation of the low-temperature reaction mechanism over Mn-doped Co_3O_4 for the selective catalytic reduction of NO_x with NH_3. J. Phys. Chem. C *119*, 22924-22933.

Hu, H., Zha, K., Li, H., Shi, L., and Zhang, D. (2016). In situ DRIFTs investigation of the reaction mechanism over MnO_x-$MO_y/Ce_{0.75}Zr_{0.25}O_2$ (M=Fe, Co, Ni, Cu) for the selective catalytic reduction of NO_x with NH_3. Appl. Surf. Sci. *387*, 921-928.

Huang, L., Hu, X., Yuan, S., Li, H., Yan, T., Shi, L., and Zhang, D. (2017). Photocatalytic preparation of nanostructured MnO_2-$(Co_3O_4)/TiO_2$ hybrids: The formation mechanism and catalytic application in SCR deNO_x reaction. Appl. Catal. B. *203*, 778-788.

Huang, L., Zha, K., Namuangruk, S., Junkaew, A., Zhao, X., Li, H., Shi, L., and Zhang, D. (2016). Promotional effect of the TiO_2 (001) facet in the selective catalytic reduction of NO with NH_3: in situ DRIFTS and DFT studies. Catal. Sci. Technol. *6*, 8516-8524.

Li, P., He, C., Cheng, J., Ma, C.Y., Dou, B.J., and Hao, Z.P. (2011). Catalytic oxidation of toluene over Pd/Co_3AlO catalysts derived from hydrotalcite-like compounds: Effects of preparation methods. Appl. Catal. B. *101*, 570-579.

Lian, Z., Liu, F., He, H., Shi, X., Mo, J., and Wu, Z. (2014). Manganese–niobium mixed oxide catalyst for the selective catalytic reduction of NO_x with NH_3 at low temperatures. Chem. Eng. J. *250*, 390-398.

Liang, H., Gui, K., and Zha, X. (2016). DRIFTS study of γFe_2O_3 nano-catalyst for low-temperature selective catalytic reduction of NO_x with NH_3. Can. J. Chem. Eng. *94*, 1668-1675.

Liu, N., Wang, J., Wang, F., and Liu, J. (2018a). Promoting effect of tantalum and antimony additives on deNO_x performance of $Ce_3Ta_3SbO_x$ for NH_3-SCR reaction and DRIFT studies. J. Rare Earths *36*, 594-602.

Liu, Z., Liu, H., Feng, X., Ma, L., Cao, X., and Wang, B. (2018b). Ni-Ce-Ti as a superior catalyst for the selective catalytic reduction of NO_x with NH_3. Mol. Catal. *445*, 179-186.

Liu, Z., Zhang, S., Li, J., and Ma, L. (2014). Promoting effect of MoO_3 on the NOx reduction by NH_3 over CeO_2/TiO_2 catalyst studied with in situ DRIFTS. Appl. Catal. B *144*, 90-95.

Ma, L., Cheng, Y., Cavataio, G., McCabe, R.W., Fu, L., and Li, J. (2014). In situ DRIFTS and temperature-programmed technology study on NH_3-SCR of NO_x over Cu-SSZ-13 and Cu-SAPO-34 catalysts. Appl. Catal. B *156-157*, 428-437.

Reddy, B.M., Khan, A., Yamada, Y., Kobayashi, T., Loridant, S., and Volta, J. (2003). Raman and X-ray Photoelectron Spectroscopy Study of $CeO_2{-}ZrO_2$ and $V_2O_5/CeO_2{-}ZrO_2$ Catalysts. Langmuir *19*, 3025-3030.

Sun, C., Liu, H., Chen, W., Chen, D., Yu, S., Liu, A., Dong, L., and Feng, S. (2018). Insights into the Sm/Zr co-doping effects on N_2 selectivity and SO_2 resistance of a MnO_x-TiO_2 catalyst for the NH_3-SCR reaction. Chem. Eng. J. *347*, 27-40.
Wei, L., Cui, S., Guo, H., Ma, X., and Zhang, L. (2016). DRIFT and DFT study of cerium addition on SO_2 of Manganese-based Catalysts for low temperature SCR. J. Mol. Catal. A: Chem *421*, 102-108.
Weng, X., Dai, X., Zeng, Q., Liu, Y., and Wu, Z. (2016). DRIFT studies on promotion mechanism of $H_3PW_{12}O_{40}$ in selective catalytic reduction of NO with NH_3. J. Colloid Interf. Sci. *461*, 9-14.
Yan, L., Liu, Y., Zha, K., Li, H., Shi, L., and Zhang, D. (2017). Scale-activity relationship of MnO_x-FeO_y nanocage catalysts derived from prussian blue analogues for low-temperature NO reduction: Experimental and DFT studies. ACS Appl. Mater. Interfaces. *9*, 2581-2593.
Zhang, H., Zou, Y., and Peng, Y. (2017). Influence of sulfation on CeO_2-ZrO_2 catalysts for NO reduction with NH_3. Chinese J. Catal. *38*, 160-167.
Zhang, Y., Yue, X., Huang, T., Shen, K., and Lu, B. (2018). In situ DRIFTS studies of NH_3-SCR mechanism over V_2O_5-CeO_2/TiO_2-ZrO_2 catalysts for selective catalytic reduction of NO_x. Materials *11*.
Zhao, W., Dou, S., Zhang, K., Wu, L., Wang, Q., Shang, D., and Zhong, Q. (2019). Promotion effect of S and N co-addition on the catalytic performance of V_2O_5/TiO_2 for NH_3-SCR of NO_x. Chem. Eng. J. *364*, 401-409.